

1  
2  
3  
4  
5  
6  
7  
8  
9  
10  
11  
12  
13  
14  
15  
16  
17  
18  
19  
20  
21  
22  
23  
24  
25  
26  
27  
28  
29  
30  
31  
32  
33  
34  
35  
36  
37  
38  
39  
40  
41  
42  
43  
44  
45  
46  
47  
48  
49  
50  
51  
52  
53  
54  
55  
56  
57  
58  
59  
60  
61  
62  
63  
64  
65

# Optimizing the design of a bioabsorbable metal stent using computer simulation methods

J. A. Grogan, S. B. Leen, P. E. McHugh

Biomechanics Research Centre (BMEC), Mechanical and Biomedical Engineering, College of  
Engineering and Informatics, NUI Galway, Ireland.

Email: [j.grogan1@nuigalway.ie](mailto:j.grogan1@nuigalway.ie) (J. A. Grogan)

**Abstract**

Computer simulation is used extensively in the design of permanent stents. In order to address new challenges that arise in the design of absorbable metal stents (AMS's), such as corrosion and the limited mechanical properties of bioabsorbable alloys, new simulation and design techniques are needed. In this study a new method for simulating AMS corrosion is developed to study the effects of corrosion on the mechanical performance of a range of stent designs. The corrosion model is combined with an optimization strategy to identify AMS features that give optimal corrosion performance in the body. It is found that strut width is the predominant geometrical factor in determining long-term AMS scaffolding performance. An AMS with superior scaffolding performance to a commercial design is identified, based on deployment and corrosion simulations in stenosed vessels. These simulation and design techniques give new insights into in-vivo AMS performance and the role of device geometry in determining long-term scaffolding performance.

Keywords: Finite element analysis; Biodegradation; Corrosion; Magnesium; Pitting; Stent

## 1 Introduction

Absorbable metal stents (AMS's) are small scaffolds for blood vessels that gradually dissolve in the body. AMS's based on magnesium alloys have shown promise in the treatment of coronary heart disease in clinical trials [1,2] and have the potential to reduce some of the long term health risks associated with permanent stents, such as in-stent restenosis [3] and late stent thrombosis [4].

Computer simulation has been used extensively in the development of permanent stents [5–9]. While many existing simulation and design techniques for stents can be applied to the AMS development, new techniques are required to account for the corrosion that the devices are subject to *in-vivo*. Grogan et al. [10] developed a continuum damage based corrosion model for AMS design which simulated uniform and localized (pitting) corrosion by modifying the mechanical properties of corroded regions of the stent. The model was calibrated and validated based on the results of immersion experiments on thin AZ31 alloy foils in Hank's solution. Gastaldi et al. [11] developed a similar continuum damage model for AMS applications, which simulated the effects of uniform and stress-mediated corrosion. In the present study, a new method for simulating device corrosion is developed which explicitly tracks the changing geometry of the stent as it corrodes, using adaptive meshing. The method is implemented in the commercial finite element (FE) solver Abaqus/Standard, and is more computationally efficient than previously developed continuum damage techniques, which use the Abaqus/Explicit solver. This superior efficiency allows corrosion to be included in parameter and optimization studies which require a large number of simulations.

Optimization techniques have proven useful in the identification of stent designs with desirable attributes [12–14]. Grogan et al. [15] have shown that the use of such techniques is of particular importance in AMS design, owing to limitations in the mechanical properties of currently available bioabsorbable alloys. Wu et al. [12] developed an optimization strategy for 2-D AMS geometries that used deployment simulations of single stent hinges, without corrosion. In the present study, a new optimization strategy for 3-D AMS design is developed which explicitly accounts for corrosion effects. This strategy, for the first time, enables the use of direct measures of long-term stent performance (i.e. long-term radial stiffness) in the optimization process. In addition, the strategy allows more accurate predictions of the stress and strain states in the device during deployment than previous studies; these measures are key constraints in the optimization process.

The premature loss of scaffolding due to corrosion has been reported to be a primary reason for the relatively poor device efficacy in the first AMS clinical trial in coronary applications [1]. Since these reports, significant efforts have been made to improve device performance through the development of bioabsorbable alloys with improved mechanical properties and corrosion resistance, as reviewed by Moravej and Mantovani [16]. Despite this, the role of device design in determining long-term scaffolding behaviour has been largely overlooked and little has been reported on either the effects of corrosion on AMS mechanical behaviour or the extent to which device performance can be improved through design modifications.

Grogan et al. [10] have predicted late lumen loss in simulations of a single AMS design undergoing uniform and pitting corrosion in a stenosed vessel, while Wu et al. [17] have predicted lumen loss for three designs undergoing stress-mediated corrosion in a vessel. The results of both studies, however, are specific to the properties of the vessels and stent geometries

used, and in the case of Wu et al. [17], to an assumed dependence of alloy corrosion behaviour on stress. Hence, these studies do not give general insights into the effects of corrosion on AMS mechanical behaviour or designs that give optimal performance. In the present study, existing and newly developed simulation and design techniques are used to investigate the effects of corrosion on the scaffolding ability of a range of stent unit-cell geometries. The results give new insights into: i) how corrosion affects scaffolding for a range of designs, loading scenarios and alloy mechanical and corrosion properties and ii) the extent to which AMS design can improve performance.

In summary, few techniques have been developed for simulating AMS corrosion [10,11] or designing AMS's [17]. New simulation and design techniques are developed here with advantages in terms of computational efficiency and the ability to account for corrosion in identifying favourable AMS designs. The objective of this study is to apply these newly developed techniques to understand the relationship between device geometry and long-term scaffolding performance and hence optimize AMS design.

## 2 Methods

Finite deformation kinematics is assumed in all finite element (FE) simulations in this work. For stents and hinges, elasticity is considered linear and isotropic in terms of finite deformation quantities (Cauchy stress and Lagrangian strain) and is described through Young's modulus ( $E$ ) and Poisson's ratio ( $\nu$ ), while plasticity is described using  $J_2$  flow theory with isotropic hardening. A new method for simulating AMS corrosion based on Arbitrary Lagrangian Eulerian (ALE) adaptive meshing is first presented. This ALE corrosion model is used in investigating the corrosion behaviour of a range of AMS designs, by means of parameter studies. A new

1  
2  
3  
4 optimization strategy is then presented, which uses the efficient global optimization (EGO)  
5  
6 algorithm [18] and the ALE corrosion model. This strategy is used to identify features of AMS  
7  
8 designs with favourable long-term performance.  
9

10  
11  
12 Following this, the deployment of a number of AMS designs in physiologically representative  
13  
14 vessel geometries is simulated to investigate how predictions of *in-vitro* AMS performance are  
15  
16 related to performance in more realistic geometries. The Abaqus/Explicit solver and the  
17  
18 continuum damage model developed in Grogan et al. [10] are used to simulate device corrosion  
19  
20 in this case, due to their favourable robustness in the treatment of simultaneous large  
21  
22 deformations, intermittent large sliding contact and corrosion.  
23  
24  
25

26  
27  
28 In all simulations the stent strut thickness is regarded as the radial device dimension (i.e. the  
29  
30 precursor tubing wall thickness for laser cut stents less any material removal during processing).  
31  
32 Width is taken as the circumferential dimension of the strut.  
33

## 34 35 36 **2.1 ALE corrosion model**

37  
38 Corrosion is simulated using the ALE adaptive meshing capability in Abaqus/Standard. This  
39  
40 capability allows the boundaries of the FE mesh to be moved independently of the underlying  
41  
42 material between analysis increments. This simulates the effects of material removal, as any  
43  
44 material outside of the FE mesh in an increment does not contribute to mechanical behaviour  
45  
46 (Abaqus Analysis Manual; [19]).  
47  
48  
49

50  
51  
52 The ALE corrosion model uses a newly developed facet based approach to track the corrosion  
53  
54 surface as it evolves over time, based on the use of 3-D linear reduced integration elements  
55  
56 (C3D8R). This approach allows corrosion to be simulated on the complex geometrical features,  
57  
58 such as corners and edges, present in the stent geometry. Here, facets are triangles whose vertices  
59  
60  
61

are given by nodes on intersecting element edges (see Supplementary Figure S1). As shown schematically in Fig. 1, uniform corrosion is simulated by moving facets along their inward pointing normals,  $\mathbf{n}$ , at a velocity equal to the corrosion rate,  $v$  (in the form  $L.T^{-1}$ ). Using this approach, the position of a node on the corrosion surface at any time can be found by finding the intersection of its corresponding facets.

The ALE corrosion model is implemented in the Abaqus/Standard code by means of a number of user subroutines. A flowchart for the implementation is given in Supplementary Figure S2. Based on the results of a mesh convergence study, all stent simulations use six C3D8R elements through the strut width.

## 2.2 *Effects of corrosion on AMS performance*

It is of interest to determine: i) the effects of corrosion on AMS mechanical performance and ii) the extent to which long-term scaffolding performance depends on device design and alloy mechanical and corrosion properties. These are investigated through two parameter studies (*P1* and *P2*) and an optimization study (*O1*). The Abaqus/Standard implicit solver is used in all three of these studies, with corrosion simulated using the ALE corrosion model.

### 2.2.1 *Parameter Study (P1)*

Parameter study *P1* focuses on a simple, sinusoidal stent hinge profile with a number of different cross-sections, shown in Fig. 2 (a). The deformation and corrosion of the hinges is simulated as shown in Fig. 2 (b) and Supplementary Movie 1. The quantity of interest in terms of hinge performance is radial stiffness ( $R_k$ ) which is taken as the slope of the initial linear portion of the force-diameter curve during crushing, normalized by the hinge length. The points used for the slope calculation on a typical force-diameter curve are shown in Supplementary Figure S3 (a).

Three elastic-plastic magnesium alloy behaviours are adopted for the hinges, shown in Tables 1 and 2, based on properties of AZ31 alloy, WE43 alloy and MZX alloy. The latter two alloys have been used in *in-vivo* AMS experiments in Erbel et al. [1] and Deng et al. [20], respectively. Elastic-plastic properties of iron are also considered, based on its use in early *in-vivo* AMS experiments [21]. The specific goals of this study are to investigate: i) the extent to which hinges consisting of different materials lose mechanical integrity with corrosion and ii) the extent to which hinges of different cross-sectional areas lose mechanical integrity with corrosion.

### 2.2.2 Parameter Study (P2)

Parameter study *P2* uses a similar approach to study *P1*, but rather than investigating a single sinusoidal hinge profile, a range of hinge profiles that are more reflective of those used in commercial AMS's, namely the DREAMS stent [2], are investigated. In this study the dimensions of the device are allowed to vary within a specified design space, shown in Fig. 3 (a). The upper bounds on the design space are due to geometrical limitations for device construction or, in the case of thickness, the desire to not increase strut thickness beyond that of early generation permanent stents (e.g. the CYPHER stent). Lower bounds correspond to hinge dimensions below which optimal designs are deemed unlikely to be found. A structured meshing technique with exactly six elements maintained through the strut width is used to ensure consistent mesh characteristics for all designs. The goals of this study are to: i) investigate the extent to which hinges with a range of different profiles lose mechanical integrity with corrosion and ii) identify a set of baseline designs to be compared with a design from a subsequent optimization study over the same design space. In the present study a Monte-Carlo based sampling method is used to generate stent designs within the design space, based on a uniformly distributed random selection of dimensions. The mechanical behaviour of AZ31 alloy, shown in



Table 2, is adopted for all simulations. Only designs with predicted maximum strains during deployment below 80% of strain at UTS are considered.

### 2.2.3 Optimization Study (O1)

In optimization study *O1* a strategy is developed to maximize the long-term scaffolding performance of a candidate AMS design by explicitly considering the effects of corrosion on device performance. The approach used incorporates the EGO algorithm [18], which is implemented in the open-source DAKOTA optimization toolkit (Sandia National Laboratories, USA). The implementation of the EGO algorithm in DAKOTA is detailed in the DAKOTA Theory Manual [22] and in Bichon et al. [23].

For the purposes of this study, the goal is to maximize hinge radial stiffness after a specific amount ( $vt = 10 \mu\text{m}$ , where  $t$  is immersion time) of corrosion. Optimizations are performed using the same design space as was used in study *P2*, shown in Fig. 3 (a). The objective function to be minimized is:

$$OF(\mathbf{x}) = 1 - AR_K(\mathbf{x}) \quad (1)$$

where  $\mathbf{x}$  is a vector with the values of the six design variables ( $L_1, L_2, L_3, H_2, W, T$ ) as its components and  $A$  is a scaling parameter. A penalty condition similar to that used in previous stent optimization studies, such as De Beule et al. [24], is used in the present study to ensure that the objective function value is relatively high when strains in a candidate hinge exceed a desired limit. The penalty condition is enforced by assigning the objective function the following value:

$$OF(\mathbf{x}) = 1 + \varepsilon(\mathbf{x}) \quad (2)$$

1  
2  
3  
4 if the predicted maximum principal logarithmic strain,  $\epsilon$ , for a hinge exceeds 80% of the strain at  
5  
6 UTS. The use of the penalty condition introduces a discontinuity in the objective function value  
7  
8 for designs with strains near the critical value. The scaling parameter  $A$  is introduced in Eqn. 1 to  
9  
10 ensure that the extent of the discontinuity is enough to enforce the desired constraint but not  
11  
12 excessive such that optimal solutions are not reliably identified. For the present study, given that  
13  
14 the strain in Eqn. 2 and radial stiffness in Eqn. 1 are not normalized in the objective function, a  
15  
16 value of 0.15 for the scaling parameter  $A$  is found to be suitable for ensuring that only designs  
17  
18 with maximum strains below the prescribed limit are identified as optimal.  
19  
20  
21  
22  
23  
24

25 The optimization can be described in five steps. In the first step, 28 initial values of  $\mathbf{x}$  are  
26  
27 randomly generated using a Latin Hypercube [25] based sampling technique. This step is  
28  
29 proposed for starting the EGO algorithm in Bichon et al. [23]. In the second step a stent  
30  
31 geometry and FE model are automatically generated for each  $\mathbf{x}$  using Python scripting and the  
32  
33 Abaqus/CAE pre-processor. In the third step the deployment, corrosion and crimping simulations  
34  
35 shown in Fig. 2 (b) are performed for each model. In the fourth step the objective function is  
36  
37 evaluated using Eqns. 1 and 2 and passed to DAKOTA. In the fifth step DAKOTA uses a best-fit  
38  
39 model (Gaussian Process surrogate model; see Bichon et al. [23] for details and Pant et al. [13]  
40  
41 for an application of this model in stent optimization) to attempt to describe  $OF$  throughout the  
42  
43 entire design space based on known discrete values of the function at previously sampled points  
44  
45  $\mathbf{x}$  (for the first iteration the 28 initial sample points are used). A new value of  $\mathbf{x}$  is identified that  
46  
47 maximises the value of an expected improvement function (EIF, as defined in Bichon et al. [23])  
48  
49 by using the best fit model and its prediction of  $OF$ . This new  $\mathbf{x}$  corresponds to a promising  
50  
51 region of the design space or a region that warrants further exploration. The optimization  
52  
53  
54  
55  
56  
57  
58  
59  
60  
61  
62  
63  
64  
65

algorithm iterates by passing this value of  $\mathbf{x}$  back into the second step and calculating the exact value of  $OF$  at this point, which is used to update the best-fit model for the next iteration. As the algorithm iterates, the uncertainty in the  $OF$  predictions by the best-fit model through the design space, and the associated EIF value, reduce and an optimal set of values of  $\mathbf{x}$  is identified.

In the present study the optimization is performed for a fixed number of iterations (150), rather than using a specific convergence criterion. This approach is found to be a suitable trade-off for obtaining a significantly improved performance over the baseline design without the additional computational expense, and diminishing returns, of specifically identifying a globally optimal solution. For the present study, the optimization process is conducted five times, in each case with a different set of twenty eight initial points. The optimal design is identified as the one with the lowest objective function value from the five optimizations. Optimizations are performed autonomously on a HPC cluster, each requiring approximately 120 CPU hours. The optimization process is performed in a sequential manner on the HPC cluster. For practical implementation reasons this is judged to be preferable for this study to the use of a parallel updating scheme, which would involve steps two, three and four being performed in parallel for multiple sample points. A parallel updating scheme for the EGO algorithm is detailed in Horowitz et al. [26].

### ***2.3 Effects of corrosion on in-vivo AMS performance***

It is of interest to investigate how improvements in AMS performance identified in study *O1* translate to improvements in predicted *in-vivo* performance. It is also of interest to predict and compare the performances of different AMS designs and a permanent stent *in-vivo*. To this end, the performance of the optimized design is compared to that of: i) a baseline design from study *P2*, ii) an approximation of a commercial AMS design (MAGIC Stent, BIOTRONIK) and iii) an

approximation of a commercial permanent stent design (OMEGA Stent Platform, Boston Scientific), in stenosed vessel geometries. The approximations of the commercial AMS and permanent stent are shown in Fig. 3 (b). The baseline design is chosen as the design with an  $R_k$  value closest to the mean of all of those found in study *P2*. All AMS designs are assumed to consist of AZ31 alloy, while the permanent stent material is modelled as PtCr, with mechanical properties shown in Tables 1 and 2.

Following the recommendations of Conway et al. [27] with regard to the representation of vessel curvature and the inclusion of a lesion in stent deployment simulations, two vessel configurations are used to simulate deployment and corrosion, shown in Fig. 4. For the curved artery, the angle  $\varphi$  corresponds to that recommend by the FDA [8] for computational studies on stents (radius of curvature = 15 mm). The delivery system, shown in Fig. 4 consists of a HDPE catheter, nitinol guide-wire and folded nylon angioplasty balloon. Important dimensions and material properties for each component are listed in Table 3. The construction of the folded angioplasty balloon geometry is detailed in Supplementary Figure S4 (a). The method of construction used is more straightforward than previously used techniques [7, 10, 28], and allows greater flexibility in choosing the balloon design. The dimensions ( $b_1, b_2, c$ ) of the balloon are chosen to produce an inflated diameter of 3.00 mm at an internal pressure of 1.2 MPa.

Arteries are assumed to consist of three layers; intima, media and adventitia. Each layer is modelled using an anisotropic hyperelastic material model by Holzapfel et al. [29], which captures the effects of helically wound collagen fibres in the tissue. The application of this model in a similar stent deployment simulation is discussed in detail in Mortier et al. [7]. The model has the following strain energy function  $\psi$ :

$$\psi = \kappa \frac{(J-1)^2}{2} + \mu(\bar{I}_1 - 3) + \frac{k_1}{2k_2} \sum_{i=4,6} (\exp[k_2\{(1-\rho)(\bar{I}_1 - 3)^2 + \rho(\bar{I}_i - 1)^2\}] - 1) \quad (3)$$

where  $\bar{I}_1 = \text{tr} \bar{\mathbf{C}}$  is the first invariant of the modified right Cauchy-Green tensor  $\bar{\mathbf{C}} = \bar{J}^{\frac{2}{3}} \mathbf{C}$ , with the volume ratio  $J = (\det \mathbf{C})^{\frac{1}{2}} > 0$  and the right Cauchy-Green tensor  $\mathbf{C}$ .  $\bar{I}_4 = \bar{\mathbf{C}} : \mathbf{M} \otimes \mathbf{M}$  and  $\bar{I}_6 = \bar{\mathbf{C}} : \mathbf{M}' \otimes \mathbf{M}'$  are two modified invariants which account for anisotropic behaviour. The direction vectors  $\mathbf{M}$  and  $\mathbf{M}'$  are described by the angle between the fibre and circumferential directions in the tubular arteries,  $\alpha$ .  $\kappa$  is a quantity related to the bulk modulus that is determined through numerical experiments, as per Mortier et al. [7]. Values for all parameters ( $\mu, k_1, k_2, \rho, \alpha, \kappa$ ) and artery layer thicknesses are included in Table 4. The model is implemented in Abaqus/Explicit by means of the user-written VUANISOHYPER subroutine.

An atherosclerotic plaque is included in the vessel, the material behaviour of which is described through an isotropic reduced order polynomial hyperelastic equation previously used in Grogan et al. [10] and calibrated in Gastaldi et al. [30], based on the results of experimental plaque characterisation by Loree et al. [30]. The model has the following strain energy function:

$$\psi = C_{10}(\bar{I}_1 - 3) + C_{20}(\bar{I}_1 - 3)^2 + C_{30}(\bar{I}_1 - 3)^3 + C_{40}(\bar{I}_1 - 3)^4 + C_{50}(\bar{I}_1 - 3)^5 + C_{60}(\bar{I}_1 - 3)^6 + \kappa \frac{(J-1)^2}{2} \quad (4)$$

with constants  $C_{i0}$  and  $\kappa$  given in Table 4. As per [27] and [30], perfect plasticity is assumed for the plaque once von Mises stresses reach 0.4 MPa. The geometry of the plaque is shown in Fig. 4 and in further detail in Supplementary Figure 4 (b) and consists of an eccentric, oval shaped lumen. The eccentricity, shape and area of the lumen change along the plaque length according to a Hicks-Henne bump function [32], following a generalisation of the method outlined in Pant

et al. [13]. The shape of the lumen corresponds to a maximum stenosis of 67 % by area, which is similar to that used in the studies of Pant et al. [13] (64 %) and Conway et al. [27] (50 to 60 %).

The length of the modelled arterial segment is 54.0 mm. Each end of the segment is fixed throughout the simulation. For the straight vessels the guide-wire is fixed in position and deployment is achieved through the application of a pressure to the inner surface of the balloon. For the curved vessel, the catheter, balloon and stent are first tracked through the vessel, followed by the application of a pressure to the inner surface of the balloon. The guide-wire is fixed at one end only in this case.

Following device deployment and recoil, the AMS geometries undergo corrosion using the uniform and pitting continuum damage corrosion models developed in Grogan et al. [10], summarized in the next section. Deployment and recoil stages for simulations in vessel geometries are performed using the Abaqus/Explicit solver and require approximately 800 CPU hours each in straight vessels and 1300 CPU hours in curved vessels. Corrosion stages are also performed using the Abaqus/Explicit solver and require approximately 400 CPU hours each. Simulations are performed on a SGI-Altix HPC cluster at the Irish Centre for High Performance Computing.

## ***2.4 Corrosion Damage Model***

The continuum damage corrosion model introduced in the previous section was developed in Grogan et al. [10] and is described in detail in that study. For completeness it is described in brief here. In this approach, elements in the FE mesh that are deemed to be exposed to the corrosive environment undergo damage. The damage acts on the element by gradually reducing its load bearing capacity over time. Eventually, a critical amount of damage in the element is reached

and it is removed from the FE mesh. This exposes new elements to the corrosive environment, which themselves begin to undergo damage.

In this study two types of corrosion are considered: i) uniform corrosion, where similar corrosion rates are assumed in every exposed element and ii) pitting corrosion, where corrosion proceeds at a higher rate in certain regions. In both cases the temporal evolution of damage in an element,  $D_e$ , is:

$$\frac{dD_e}{dt} = \frac{\delta_U}{L_e} \lambda_e k_U \quad (5)$$

where  $k_U$  is a corrosion kinetic parameter and  $\delta_U$  and  $L_e$  are respective material and element characteristic lengths [10].

For the uniform corrosion model the remaining parameter  $\lambda_e$  is set equal to 1.0, and it is possible to replace the product  $\delta_U k_U$  with  $v$  (which is equivalent to the corrosion rate parameter used in the ALE corrosion model). Since  $L_e$  is simply a property of the FE mesh, this allows the uniform corrosion damage model to be calibrated with a single parameter,  $v$ . The predictions of the ALE corrosion model and the uniform corrosion damage model can then be presented in terms of the quantity,  $vt$ , which is the input corrosion rate multiplied by the immersion time and can be considered to be an equivalent one-dimensional ‘corrosion distance’. Using this quantity means that results are applicable for any uniformly corroding alloy (not just AZ31), once the corrosion rate for that alloy is known. A further advantage of using this quantity is that results expressed in this form are applicable even when the input corrosion rate is not constant in time (if  $vt$  is interpreted as  $\int_0^t v(t) dt$  in that case).

For the pitting corrosion model, random  $\lambda_e$  values are assigned to initially exposed elements using a standard Weibull distribution. Through adjusting the shape parameter,  $\gamma$ , of the Weibull distribution, the degree of localization of the pitting process can be controlled. For this model, once elements become exposed they inherit the  $\lambda_e$  value of their recently removed neighbouring element,  $\lambda_n$ , according to:

$$\lambda_e = \beta \lambda_n \quad (6)$$

where  $\beta$  is a dimensionless parameter that depends on  $L_e$  according to:

$$\beta = \beta_0 \frac{L_e}{L_{e,0}} \quad (7)$$

and  $\beta_0 = 0.8$  and  $L_{e,0} = 0.07$  are reference values from [10].  $\beta$  controls how quickly a corrosion pit will grow, with higher values resulting in more rapid pit growth. For the pitting model the parameters  $k_U = 0.00042 \text{ hr}^{-1}$ ,  $\delta_U = 0.017 \text{ mm}$  and  $\gamma = 0.2$  are taken from Grogan et al. [10]. In Grogan et al. [10] these values were determined based on the calibration of the model such that it captured the experimentally observed corrosion behaviour of AZ31 alloy foils in Hank's solution. Model predictions using these parameters were subsequently validated against the results of an independent experiment. Random  $\lambda_e$  values are assigned by placing a virtual grid with cuboidal cells of side length  $L_{e,0}$  over the mesh in a pre-processing step. Each cell is assigned a random  $\lambda_e$  value from a standard Weibull distribution with shape parameter  $\gamma$  and each element of the mesh within that cell assumes its  $\lambda_e$  value.



### 3 Results

#### 3.1 Parameter and Optimization Studies

Fig. 5 (a) shows the predicted reduction in  $R_k$  and maximum radial force in a corroding hinge from study *P1*. Individual force-diameter curves for the hinge after various amounts of corrosion are shown in Supplementary Figure S3 (a). In Fig. 5 (a) the reductions in stiffness and maximum force with corrosion are initially linear, with the rate of loss of both decreasing gradually with increasing corrosion. Fig. 5 (b) shows the initial  $R_k$  of hinges with a variety of cross-section profiles. As is expected, wider struts have greater radial stiffness. Fig. 5 (c) shows predicted stiffness retention, or the stiffness of the device during corrosion,  $R_k$ , divided by the stiffness before corrosion,  $R_{k,0}$ , for a variety of hinge profiles and materials. The stiffness retention is quite similar in each hinge, regardless of underlying material. However, there is slightly greater stiffness retention in hinges with larger circumferential widths.

Fig. 5 (d) shows the loss in  $R_k$  with corrosion for a sample of the geometries considered in parameter study *P2* ( $n = 25$ ) and the optimized design from optimization study *O1* (denoted Opt 5 in Table 5). The optimization process leads to a design with significantly higher  $R_k$  than is predicted in the designs assessed in parameter study *P2*, before and during corrosion. As per study *P1* in Fig. 5 (c), there is similar stiffness retention with corrosion for all the parameter study *P2* designs. However, there is better stiffness retention in the optimized design than the *P2* designs for most of the corrosion process (shown in Supplementary Figure S3 (b)). The reason for the improved performance of the optimized design can be seen when the device dimensions, shown in Table 5, and the results shown in Fig. 5 (b) and Fig. 5 (c) are considered. From Table 5, a general feature of the optimal designs identified in each of the five optimizations performed,

and in particular the overall optimal design (Opt 5), is that strut widths are significantly greater than those of the baseline design (143 vs. 114  $\mu\text{m}$  for Opt 5). Fig. 5 (b) indicates that struts with greater width have greater initial radial stiffness and Fig. 5 (c) shows that struts with greater width have greater stiffness retention. Thus, greater AMS strut width is expected to give better scaffolding performance before and during corrosion. It is noted that the improvement in stiffness retention in the optimal design over the baseline is smaller than the variation in Fig. 5 (c). This is because no limitation on maximum hinge strain is adopted in study *PI* while there is a limitation in the optimization study, thus limiting the range of allowable hinge profiles.

### 3.2 *In-vivo deployment simulations*

The simulated deployment of a stent in a straight arterial configuration is shown in Supplementary Movie 2. The simulated tracking of a stent and catheter through a curved stenosed vessel and subsequent deployment is shown in Supplementary Figure S5 (a). The simulated uniform corrosion of a stent is shown in Supplementary Movie 3. Fig. 6 (a) shows cross-sections of predicted stent configurations before and after uniform corrosion for  $vt = 37.5$   $\mu\text{m}$ . Device collapse is, expectedly, most notable in regions with the highest degree of initial occlusion. Fig. 6 (b) shows a profile of lumen area along the length of the plaque before stenting, at maximum balloon inflation and after device recoil and corrosion. From this figure it is observed that the optimized AMS and the commercial permanent stent have similar predicted acute recoils. Fig. 6 (c) shows predicted reductions in MLA and mass loss with corrosion for each AMS design. For uniform corrosion, the MLA maintained by the optimized AMS is predicted to be greater than that of the baseline geometry and commercial geometry. The optimized stent is predicted to lose less mass than the baseline and commercial device for a given corrosion rate and immersion time.

Fig. 7 (a) compares cross-sections of stented arteries for uniform and pitting corrosion of the baseline geometry for a case where both have lost 15 % of their original mass. In this case it is clear that lumen loss is significantly higher in the stent undergoing pitting corrosion. Mass loss, rather than  $vt$ , is a more suitable quantity for presenting the results of the pitting model, as the predictions of this model are not uniquely specified by the quantity  $v$ , given that they also depend on the characteristics of pit initiation and growth ( $\gamma$  and  $\beta$ ). Fig. 7 (b) shows predicted lumen loss for stents undergoing uniform and pitting corrosion, with three different random pitting assignments. It is predicted that for a given amount of mass loss, lumen loss is significantly greater for all stents undergoing pitting corrosion than for those undergoing uniform corrosion. A general improvement in lumen retention is predicted for the optimized stent undergoing pitting corrosion over the baseline stent, however the extent of the improvement is small relative to the variation in scaffolding performance for different initial random pit assignments. Fig. 7 (c) shows the predicted times at which chronic recoil of the device due to corrosion leads to a 25 % stenosis by area, considering the corrosion rates of a number of typical candidate magnesium alloys. The plot allows the extent of performance improvements due to design optimization and improvements due to using different alloys to be compared. It is noted that both optimized and baseline AZ31 alloy stents undergoing pitting corrosion are predicted to reach the critical level of chronic recoil approximately 20 times faster than the same stents undergoing uniform corrosion.

For deployments in curved vessels similar lumen areas are predicted for both stents to those obtained in straight vessels, shown in Fig. 6, along with similar lumen losses with uniform corrosion for the AMS (see Supplementary Figures 5 (b) and 5 (c)). Fig. 8 shows the change in lumen curvature with stenting for the same stents. The measure of curvature used is the distance

1  
2  
3  
4 between the lumen centroid and a straight line joining the lumen centroids at each end of the  
5  
6 plaque. Straightening of the vessel is shown during deployment, with some return to the original  
7  
8 curvature evident following balloon deflation. As the AMS corrodes the curvature of the vessel  
9  
10 is predicted to approach that of the original configuration.  
11  
12  
13  
14

## 15 16 **4 Discussion**

### 17 18 19 **4.1 ALE Corrosion Model**

20  
21  
22 In this study a method for simulating the effects of uniform corrosion on stent scaffolding is  
23  
24 developed, based on adaptive meshing. The approach is more efficient than previously developed  
25  
26 damage approaches [10, 11] and, since it does not rely on element removal, less sensitive to  
27  
28 mesh resolution. The model developed in this study can be easily calibrated, relying only on a  
29  
30 knowledge of corrosion rate, and can be applied to corrosion studies on other implants, in  
31  
32 particular orthopaedic implants where large deformations are not typical. Due to the explicit  
33  
34 tracking of the corrosion surface, the model developed here can also be easily extended to model  
35  
36 corrosion in a more physical manner than previous methods. In particular, since the velocity of  
37  
38 surface facets is explicitly controlled through a user subroutine, it can depend on, for example,  
39  
40 species concentrations and fluxes at the corrosion surface and volume averaged material stresses  
41  
42 and strains in the vicinity of the corrosion surface. A limitation of the adaptive meshing approach  
43  
44 is that it is difficult to account for complex geometric interactions, for example the merging of  
45  
46 corrosion pits.  
47  
48  
49  
50  
51  
52  
53

### 54 55 **4.2 Parameter and Optimization Studies**

56  
57 A strong link between the initial and long term radial stiffness and maximum radial forces of  
58  
59 AMS's undergoing uniform corrosion is identified, based on predictions in Figs. 5 (a) and (c).  
60  
61  
62  
63  
64  
65

Results suggest that there is an initially linear loss in radial stiffness and maximum force with uniform corrosion (*vt*) in AMS hinges, with the rate of loss depending mostly on hinge circumferential width and with little dependence on alloy mechanical properties or strut cross-section shape (circular, square, rounded). This means that: i) when assessing a candidate alloy or stent design for AMS application, radial stiffness and maximum force evaluations before corrosion give a reasonable indication of long term performance, ii) a ‘first-pass’ optimization of an AMS design can simply seek to maximise radial stiffness and force without accounting for corrosion and iii) the rate of loss of stiffness and force for many stent designs and alloys due to uniform corrosion can be approximated from Figs. 5 (c) and 5 (d).

The optimization strategy developed in this study goes beyond previous AMS optimization studies [12] in that it implicitly accounts for the effects of corrosion in identifying an optimal stent geometry and uses a 3-D simulation of stent deployment for objective function evaluations. As shown in Fig. 5 (d), the optimization strategy leads to significantly improved long-term device radial stiffnesses relative to designs identified through a Monte-Carlo approach, for a similar computational expense. A particularly important feature of the optimized design is large strut width (143  $\mu\text{m}$ ), as shown in Table 5. This large width leads to a favourable initial radial stiffness and is also likely to have contributed to favourable retention of stiffness during corrosion (see Supplementary Figure S3 (b)). Based on these predictions (Fig. 5 (c) and Fig. 5 (d)) the use of struts with large widths, which interestingly weren’t used in the commercial MAGIC stent (strut width is less than 100  $\mu\text{m}$  based on SEM images in Di Mario et al. [33]), are particularly encouraged for AMS’s. It is noted, however, that the ability to identify designs with both large widths and suitable maximum deployment strains is not straightforward, due to the limited ductility of currently available magnesium alloys [15], and is only made possible through

the use of optimization methods in this study. High strut thicknesses are also encouraged, however: i) they do not contribute to increases in radial stiffness or stiffness retention to the same degree as similar increases in width and ii) feasible values of strut thickness are likely to be limited by other metrics, such as their influence on vessel haemodynamics and device deliverability [34].

### ***4.3 In-Vivo Deployment Simulations***

Through deployment simulations in stenosed vessels a number of insights into AMS performance is gained. First, the results in Figs. 5 (d), 6 (b) and 6 (c) give an appreciation of how long-term stent radial stiffness is related to lumen loss over time. This is useful as many AMS designs are likely to have radial stiffnesses that fall between those of the baseline and optimized designs in this study. Second, the predicted improvements in scaffolding duration with stent optimization, shown in Fig. 6 (c), can be directly compared to improvements gained through using alloys with different corrosion rates, which can vary over orders of magnitude [35], and through potential improvements through slowing corrosion rates through coating and surface treatments [36, 37]. A third insight is in relation to the relative performances of AMS's and permanent stents. In Grogan et al. [15] it was predicted that AMS's can match the short-term scaffolding performance of permanent stents based on the results of relatively simple deployment and crimping simulations, similar to those shown in Fig. 2 (b). In this study it is verified in Fig. 6 (b) and Supplementary Figure 5 (c) that, with careful design, the performance of a magnesium AMS can match the short-term scaffolding performance of a modern, permanent stent in complex arterial configurations, albeit with somewhat larger strut cross-sectional area.

#### 4.4 Limitations

Corrosion is treated in a phenomenological manner in this study, with a focus on its effects on device mechanical integrity. In reality, the corrosion of devices in the body is a highly complex phenomenon and can depend on alloy microstructure, surface condition, residual and cyclic stresses, stent processing and transport conditions in the vessel. Uniform corrosion is the target behaviour for AMS alloys, as it leads to predictable device performance, and as shown in Fig. 10, generally results in greatest retention of scaffolding for a given amount of mass loss. If uniform corrosion is maintained *in-vivo*, the results of this study remain applicable, even if vessel transport conditions or surface conditions lead to time dependent corrosion rates.

If uniform corrosion is not applicable, predicted stent radial stiffnesses for a given amount of mass loss may be over-estimated in this study. The extent of this over-estimation can be appreciated based on the results in Fig. 7 (b). The pitting model used in this study is calibrated based on the results of experiments in a reasonably aggressive corrosion environment [9] and its predictions are in good agreement with observed *in-vitro* stent behaviour in a similar environment [38]. It is likely, however, that the pitting results in Fig. 7 (b) (and the relevant experiments) under-estimate *in-vivo* stent scaffolding duration for a given mass loss rate somewhat. Thus, it is likely that general AMS *in-vivo* corrosion behaviour falls between predictions shown in Fig. 7 (b) for the ideal uniform corrosion behaviour and the more aggressive pitting corrosion behaviour.

In this study the time-dependent behaviour of coronary tissue is not considered. Following deployment, the tissue will gradually adapt to the presence of the stent which may reduce radial pressure on the device. Accounting for this behaviour is important in future predictions of AMS

performance and may lead to a decrease in predicted lumen loss for a given corrosion time. Despite this limitation, it is noted that the deployment simulations in vessels performed in this study are the most detailed of those performed on AMS's to date.

A potential improvement to the optimization scheme developed in this study is the use of an optimized Latin Hypercube sampling scheme, which may produce better sampling coverage of the design space and reduce the need for multiple optimizations with different seeds. An example of such an approach with the EGO algorithm is given in Horowitz et al. [26].

## 5 Conclusions

A method for modelling stent corrosion was developed based on adaptive meshing. Using this method, the radial stiffness in stents undergoing uniform corrosion was predicted to decrease as an initially linear function of the quantity 'corrosion rate multiplied by immersion time'. The rate of decrease was predicted to primarily depend on circumferential strut width and was reasonably independent of alloy mechanical properties and strut cross-section shape. For AMS's undergoing uniform corrosion it was predicted that initial design studies could avoid modelling corrosion in improving long-term scaffolding performance by focusing on maximizing radial stiffnesses and forces. Finally, an optimization process for AMS's was developed, which incorporated the effects of corrosion. Using the optimization process an AMS design was identified that was predicted to maintain lumen patency approximately 1.5 times longer than a commercial design and a baseline design.



## Acknowledgements

This research is funded through an IRCSET scholarship under the EMBARK initiative (J. A. Grogan). The authors would like to acknowledge the SFI/HEA funded Irish Centre for High End Computing for the provision of computational resources and support.

References

[1] Erbel R, Di Mario C, Bartunek J, Bonnier J, De Bruyne B, Eberli FR, et al. Temporary scaffolding of coronary arteries with bioabsorbable magnesium stents: a prospective, non-randomised multicentre trial. *Lancet* 2007;369:1869–75.

[2] Haude M, Erbel R, Erne P, Verheye S, Degen H, Böse D, et al. Safety and performance of the drug-eluting absorbable metal scaffold (DREAMS) in patients with de-novo coronary lesions: 12 month results of the prospective, multicentre, first-in-man BIOSOLVE-I trial. *Lancet* 2013; 6736:1–9.

[3] Mitra AK, Agrawal DK. In stent restenosis: bane of the stent era. *J Clin Pathol* 2006;59:232–239.

[4] Daemen J, Wenaweser P, Tsuchida K, Abrecht L, Vaina S, Morger C, et al. Early and late coronary stent thrombosis of sirolimus-eluting and paclitaxel-eluting stents in routine clinical practice: data from a large two-institutional cohort study. *Lancet* 2007;369:667–78.

[5] Etave F, Finet G, Boivin M, Boyer JC, Rioufol G, Thollet G. Mechanical properties of coronary stents determined by using finite element analysis. *J Biomech* 2001;34(8):1065–75.

[6] Migliavacca F, Petrini L, Colombo M, Auricchio F, Pietrabissa R. Mechanical behavior of coronary stents investigated through the finite element method. *J Biomech* 2002;35(6):803–11.

[7] Mortier P, Holzapfel GA, De Beule M, Van Loo D, Taeymans Y, Segers P, et al. A novel simulation strategy for stent insertion and deployment in curved coronary bifurcations: comparison of three drug-eluting stents. *Ann Biomed Eng* 2010;38(1):88–99.

[8] FDA. Non-Clinical Engineering Tests and Recommended Labeling for Intravascular Stents and Associated Delivery Systems. Online 2013. Available from URL: <http://www.fda.gov/MedicalDevices/DeviceRegulationandGuidance/PostmarketRequirements/QualitySystemsRegulations/MedicalDeviceQualitySystemsManual/ucm122416.htm>

[9] Donnelly EW, Bruzzi MS, Connolley T, McHugh PE. Finite element comparison of performance related characteristics of balloon expandable stents. *Comput Methods Biomech Biomed Engin* 2007;10(2):103–10.

[10] Grogan JA, O’Brien BJ, Leen SB, McHugh PE. A corrosion model for bioabsorbable metallic stents. *Acta Biomater* 2011;7:3523–33.

[11] Gastaldi D, Sassi V, Petrini L, Vedani M, Trasatti S, Migliavacca F. Continuum damage model for bioresorbable magnesium alloy devices - application to coronary stents. *J Mech Behav Biomed Mater* 2011;4:352–65.

- [12] Wu W, Petrini L, Gastaldi D, Villa T, Vedani M, Lesma E, et al. Finite element shape optimization for biodegradable magnesium alloy stents. *Ann Biomed Eng* 2010;38:2829–40.
- [13] Pant S, Bressloff NW, Limbert G. Geometry parameterization and multidisciplinary constrained optimization of coronary stents. *Biomech Model Mechanobiol* 2012;11:61–82.
- [14] Pant S, Limbert G, Curzen NP, Bressloff NW. Multiobjective design optimisation of coronary stents. *Biomaterials* 2011;32:7755–73.
- [15] Grogan JA, Leen SB, McHugh PE. Comparing coronary stent material performance on a common geometric platform through simulated bench-testing. *J Mech Behav Biomed Mater* 2012;12:129-138.
- [16] Moravej M, Mantovani D. Biodegradable metals for cardiovascular stent application: interests and new opportunities. *Int J Mol Sci* 2011;12:4250–70.
- [17] Wu W, Gastaldi D, Yang K, Tan L, Petrini L, Migliavacca F. Finite element analyses for design evaluation of biodegradable magnesium alloy stents in arterial vessels. *Mater Sci Eng B* 2011;176:1733-40.
- [18] Jones DR, Schonlau M, William J. Efficient global optimization of expensive black-box functions. *J Global Optim* 1998;13:455–92.
- [19] Anon., Abaqus analysis manual v6.10. Rhode Island, USA: DS SIMULIA, 2010.
- [20] Deng CZ, Radhakrishnan R, Larsen SR, Boismier DA, Stinson JS, Hotchkiss AK, et al. Magnesium alloys for bioabsorbable stents: a feasibility assessment. In: Sillekens, WH, Agnew, SR, Neelameggham, NR, Mathaudhu, SN, editors. *Magnesium technology 2011*. New Jersey: John Wiley and Sons Inc., 2011. p. 413-418.
- [21] Peuster M, Hesse C, Schloo T, Fink C, Beerbaum P, Von Schnakenburg C. Long-term biocompatibility of a corrodible peripheral iron stent in the porcine descending aorta. *Biomaterials* 2006;27:4955–62.
- [22] Anon., DAKOTA theory manual v5.2. New Mexico USA: Sandia National Laboratories, 2012.
- [23] Bichon BJ, Eldred MS, Swiler LP, Mahedevan S, McFarland JM. Multimodal reliability assessment for complex engineering applications using efficient global optimization. In: *Proceedings of the 48<sup>th</sup> AIAA/SME/ASCE/AHS/ASC structures, structural dynamics and materials conference*. Hawaii: AIAA, 2007.
- [24] De Beule M, Van Cauter S, Mortier P, Van Loo D, Van Impe R, Verdonck, P, Verhegghe B. Virtual optimization of self-expandable braided wire stents. *Med Eng Phys* 2009;31:448–53.

- [25] Santer TJ, Williams BJ, Notz, WI. The design and analysis of computer experiments. Berlin: Springer-Verlag, 2003.
- [26] Horowitz, B, Guimarães, LJDN, Dantas, V, Afonso, SMB. A concurrent efficient global optimization algorithm applied to polymer injection strategies. *J Petrol Sci Eng* 2010;71(3-4):195–204.
- [27] Conway C, Sharif F, McGarry JP, McHugh PE. A computational test-bed to assess coronary stent implantation mechanics using a population-specific approach. *Cardiovasc Eng Technol* 2012;3:374–87.
- [28] Laroche D, Delorme S, Anderson T, DiRaddo R. Computer prediction of friction in balloon angioplasty and stent implantation. In: Harders M, Szekely G, editors. *Biomedical simulation*. Berlin: Springer-Verlag, 2006. p.1-8.
- [29] Holzapfel GA, Sommer G, Gasser CT, Regitnig P. Determination of layer-specific mechanical properties of human coronary arteries with nonatherosclerotic intimal thickening and related constitutive modeling. *Am J Physiol Heart Circ Physiol* 2005;289:2048–58.
- [30] Gastaldi D, Morlacchi S, Nichetti R, Capelli C, Dubini G, Petrini L, et al. Modelling of the provisional side-branch stenting approach for the treatment of atherosclerotic coronary bifurcations: effects of stent positioning. *Biomech Model Mechanobiol* 2010;9:551–61.
- [31] Loree HM, Tobias BJ, Gibson LJ, Kamm RD, Small DM, Lee RT. Mechanical properties of model atherosclerotic lesion lipid pools. *Arterioscler Thromb Vasc Biol* 1994;14:230–4.
- [32] Hicks R, Henne P. Wing design by numerical optimization. *J Aircraft* 1978;15:407-412.
- [33] Di Mario C, Griffiths H, Goktekin O, Peeters N, Verbist J, Bosiers M, et al. Drug-eluting bioabsorbable magnesium stent. *J Interv Cardiol* 2004;17:391–5.
- [34] Pache J, Kastrati A, Mehilli J, Schuhlen H, Dotzer F, Hausleiter J, et al. Intracoronary stenting and angiographic results: strut thickness effect on restenosis outcome (ISAR-STEREO-2) trial. *J Am Coll Cardiol* 2003;41(8):1283–8.
- [35] Kirkland NT, Lespagnol J, Birbilis N, Staiger MP. A survey of bio-corrosion rates of magnesium alloys. *Corros Sci* 2010;52(2):287–91.
- [36] Wong HM, Yeung KWK, Lam KO, Tam V, Chu PK, Luk KDK, et al. A biodegradable polymer-based coating to control the performance of magnesium alloy orthopaedic implants. *Biomaterials* 2010;31(8):2084–96.
- [37] Chen Y, Song Y, Zhang S, Li J, Zhao C, Zhang X. Interaction between a high purity magnesium surface and PCL and PLA coatings during dynamic degradation. *Biomed Mater* 2011;6:1-8.

- 1  
2  
3  
4 [38] Wu W, Chen S, Gastaldi D, Petrini L, Mantovani D, Yang K, et al. Experimental data  
5 confirm numerical modeling on degradation process of magnesium alloys stents. *Acta*  
6 *Biomater* 2012; In Press. (DOI: 10.1016/j.actbio.2012.10.035).  
7  
8  
9 [39] Li N, Guo C, Wu YH, Zheng YF, Ruan, LQ. Comparative study on corrosion behaviour  
10 of pure Mg and WE43 alloy in static, stirring and flowing Hank's solution . *Corros Eng*  
11 *Sci Technol* 2012;47(5): 6.  
12  
13 [40] O'Brien BJ, Stinson JS, Larsen SR, Eppihimer MJ, Carroll WM. A platinum-chromium  
14 steel for cardiovascular stents. *Biomaterials* 2010;31:3755–61.  
15  
16 [41] Gu XN, Zhou WR, Zheng YF, Cheng Y, Wei SC, Zhong SP, et al. Corrosion fatigue  
17 behaviors of two biomedical Mg alloys - AZ91D and WE43 - in simulated body fluid.  
18 *Acta Biomater* 2010;6:4605–13.  
19  
20 [42] Islam MA, Sato N, Tomota Y. Tensile and plane bending fatigue properties of pure iron  
21 and iron-phosphorus alloys at room temperature in the air. *T Indian I Metals* 2011;64:315–  
22 20.  
23  
24  
25  
26  
27  
28  
29  
30  
31  
32  
33  
34  
35  
36  
37  
38  
39  
40  
41  
42  
43  
44  
45  
46  
47  
48  
49  
50  
51  
52  
53  
54  
55  
56  
57  
58  
59  
60  
61  
62  
63  
64  
65

Figures

**Fig. 1** Facets along the corrosion interface move inward along their normals,  $\mathbf{n}_i$ , at constant velocity,  $\mathbf{v}$ . The position of an exterior node at any time is given by the intersection of its facets.

**Fig. 2** (a) Hinge cross-sections and FE meshes and a schematic of the hinge profile are shown. All cross-sections have a radial thickness of 0.12 mm. Cross-sections 1, 4 and 6 have a circumferential width of 0.12 mm while the others have a width of 0.14 mm. The hinge profile has length ( $L_T$ ) equal to 1.1 mm and height ( $H$ ) equal to 0.785 mm. (b) Deployment and corrosion simulations for the hinges. The hinge is deployed by expanding a semi-rigid inner cylinder. It then undergoes recoil and corrosion and is subsequently crushed using an outer cylinder. Symmetry boundary conditions are used so only quarter of the stent unit is modelled.

**Fig. 3** (a) Schematic of the stent design used in the parameter and optimization studies. The profile has a fixed overall height  $H_1$ , corresponding to an outer diameter of 1.5 mm, and is extruded through an out-of-plane thickness  $T$ . (b) Designs for the MAGIC and OMEGA stent approximations used in this study. For the MAGIC stent,  $H = 1.18$  mm and  $L = 2.1$  mm. Strut width is 0.08 mm and thickness is 0.16 mm. For the OMEGA stent  $H = 2.03$  mm and  $L = 2.25$  mm. Strut width is 0.1 mm and thickness is 0.08 mm.

**Fig. 4** Stent deployment model in straight and curved arterial configurations.

**Fig. 5** (a) Reduction in  $R_k$  and maximum force in a hinge due to corrosion. (b)  $R_k$  values for a selection of hinge profiles before corrosion. (c)  $R_k$  values for a selection of hinge profiles (CS 1-6 in Fig. 7 (b)) and materials (M 2-4 in Table 1) during corrosion. (d) Predicted changes in  $R_k$  during corrosion for the optimized design and the designs in

the parameter study  $P2$ . Error bars signify one standard deviation from the mean, based on a sample of 25 stent geometries.

**Fig. 6** (a) Cross-sections of predicted stent configurations before and after uniform corrosion (for  $vt = 37.5 \mu\text{m}$ ). (b) Lumen area profiles for the optimized AMS and OMEGA stent during corrosion of the former. (c) Change in MLA and loss in mass for the optimized, baseline and commercial AMS's undergoing uniform corrosion in a straight vessel.

**Fig. 7** (a) Artery cross-section showing predictions for uniform and pitting corrosion of the baseline geometry for 15 % mass loss (b) Losses in lumen area due to stent corrosion for uniform and pitting cases. Each of the three curves for the pitting models represents a simulation of the same stent design undergoing pitting with three different random initial pit assignments. (c) Predicted immersion times required for a return to 25% stenosis by area due to corrosion, assuming AZ31 alloy ( $v = 11.0 \mu\text{m/day}$ ) [10], AZ91 alloy ( $v = 1.6 \mu\text{m/day}$ ) [35] and WE43 alloy ( $v = 5.2 \mu\text{m/day}$ ) [39] corrosion rates and uniform corrosion. The immersion time for AZ31 alloy [10] undergoing pitting corrosion is also included.

**Fig. 8** Change in vessel curvature following stenting, as measured by the distance between the lumen centroid and a straight line (centre-line) joining the lumen centroids at each end of the plaque.

## Supplementary Figures

**Fig. S1** For each node in the FE mesh,  $N$ , its corresponding facets are the triangles generated by connecting it to pairs of nodes with which it shares element edges and which occupy the same element face. For example, the facet  $F_1$  is given by the nodes,  $N$ ,  $N_1$  and  $N_2$ .

**Fig. S2** A flowchart for the implementation of the ALE corrosion model with Abaqus/Standard.

**Fig. S3** (a) Force ( $F$ ) – diameter ( $D$ ) curves for a stent hinge during crushing, following various degrees of corrosion. Radial stiffness is taken as the slope of the stent's force-diameter curve between points '1' and '2' during crushing. Maximum radial force is found at the point  $F_{max}$ . (b) The fraction of the radial stiffness before corrosion,  $R_{k,0}$ , that is maintained as the stents corrode.

**Fig. S4** (a) Schematic showing the construction of the folded angioplasty balloon. The balloon geometry is constructed by mapping the shown geometry into a cylindrical configuration. The balloon's tapered ends are constructed by reducing  $b_2$  appropriately using the 'Loft' command in Abaqus/CAE. (b) Schematic of the plaque geometry used in this study. The centre of the lumen varies eccentrically along the plaque length according to a Hickes-Henne bump function. The shape and area of the lumen gradually transition from circular to oval along the length, according to the same bump function.

**Fig. S5** (a) The simulated tracking and deployment of a stent in a vessel geometry. (b) Cross-sections of arterial segments: (1.) pre-stenting, (2.) post-stenting with the Omega stent, (3.) post-stenting with the optimized AMS and (4.) following corrosion of the AMS. (c) Lumen area profiles for the permanent stent and AMS in a curved artery during corrosion of the latter.

## Supplementary Movies

**Movie 1** The simulated deployment, corrosion and crushing of a stent hinge. Corrosion is simulated using the ALE corrosion model.

**Movie 2** The simulated deployment of a stent in a stenosed straight vessel geometry. A realistic 'dog-boning' behaviour is observed.

**Movie 3** The simulated uniform corrosion of a stent in a stenosed straight vessel geometry. Corrosion is simulated using the corrosion damage model.

Figure1

[Click here to download high resolution image](#)

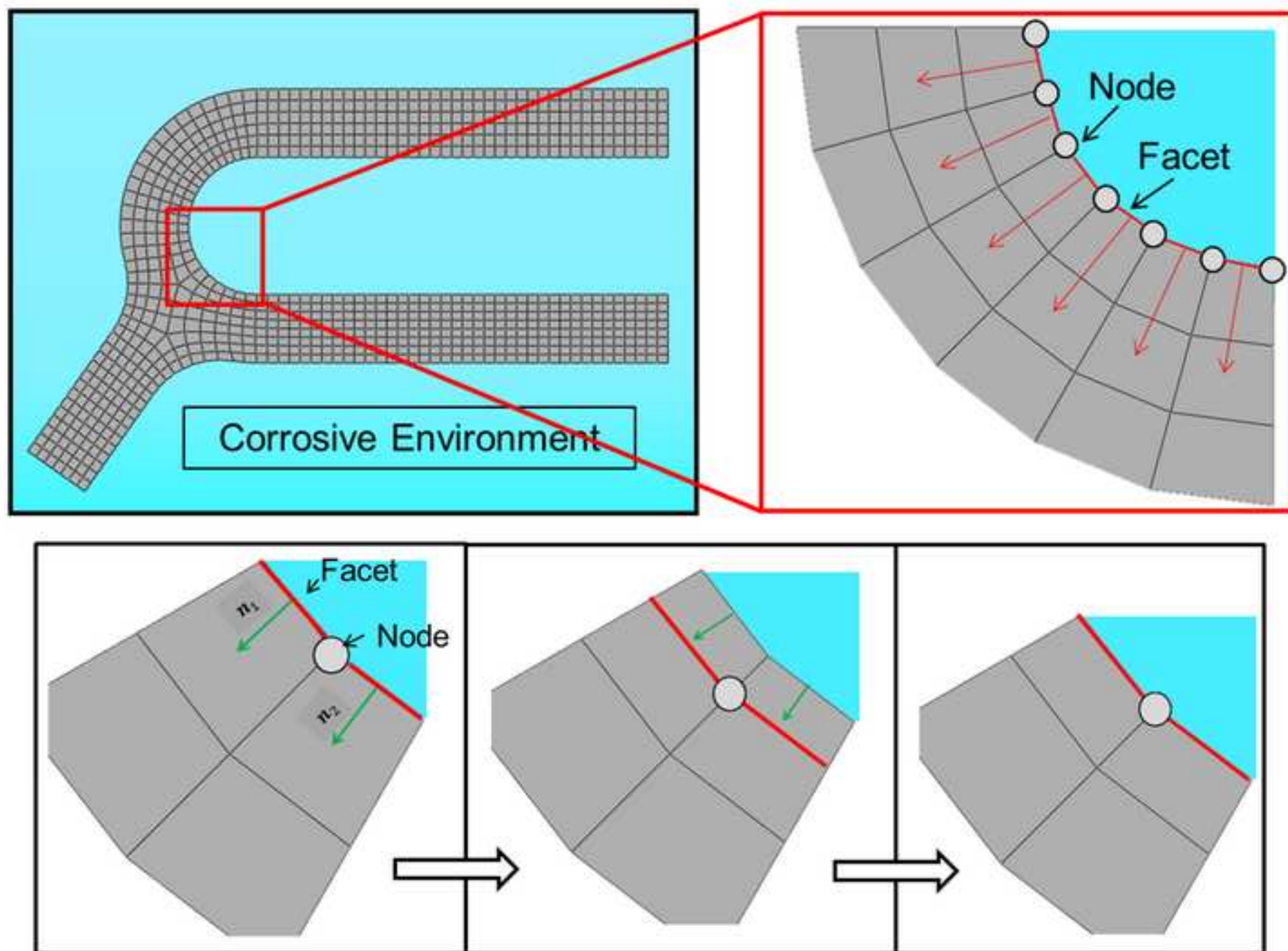




Figure 2a  
[Click here to download high resolution image](#)

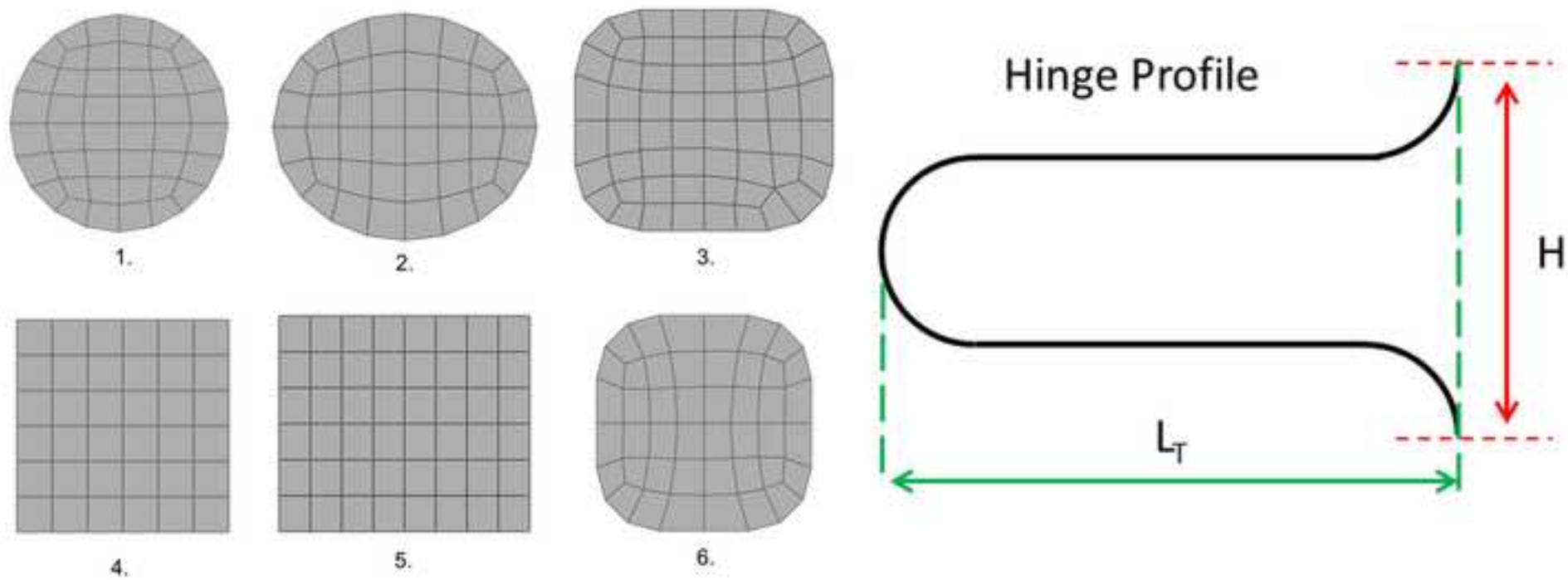


Figure 2b  
[Click here to download high resolution image](#)

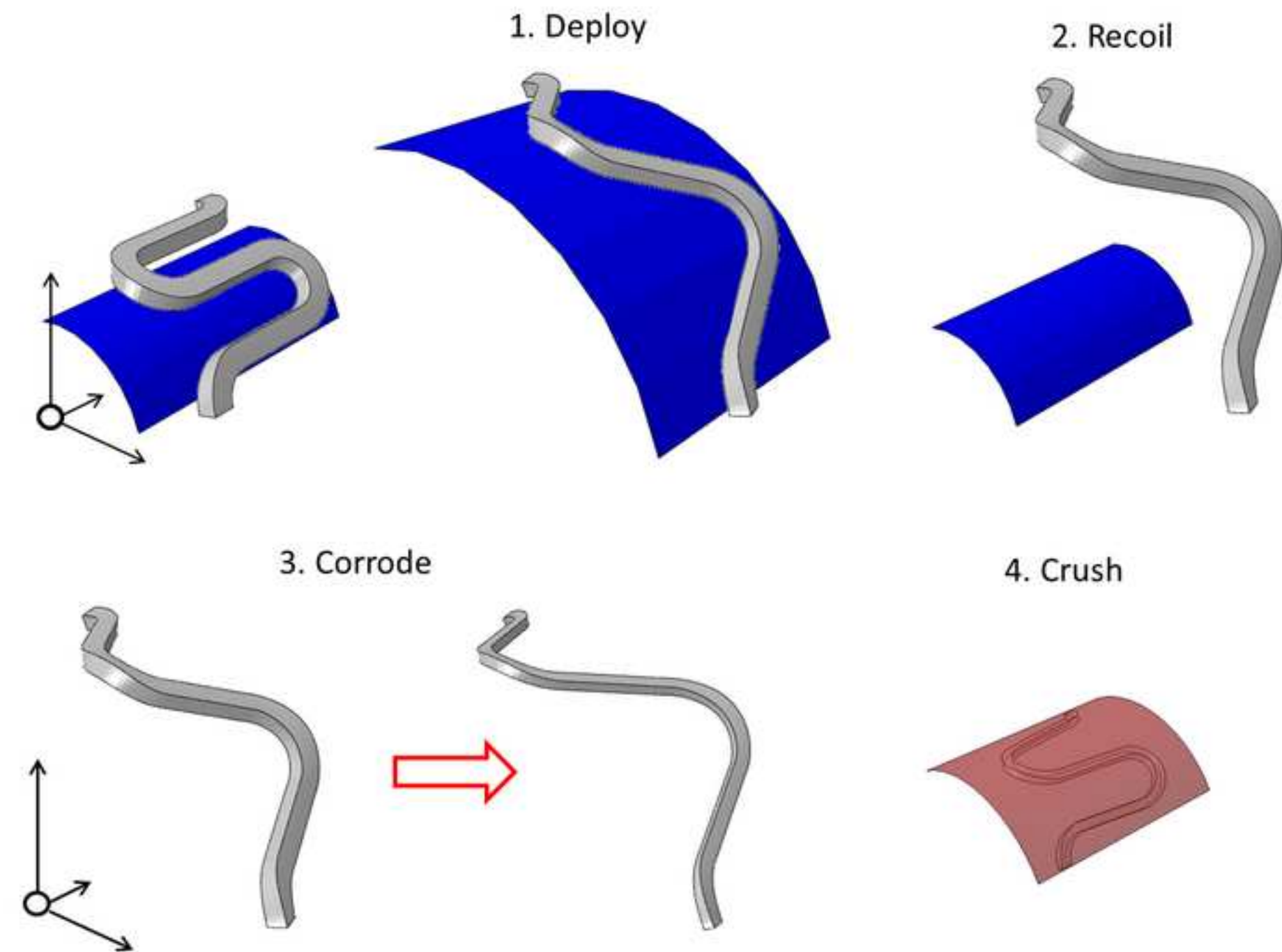
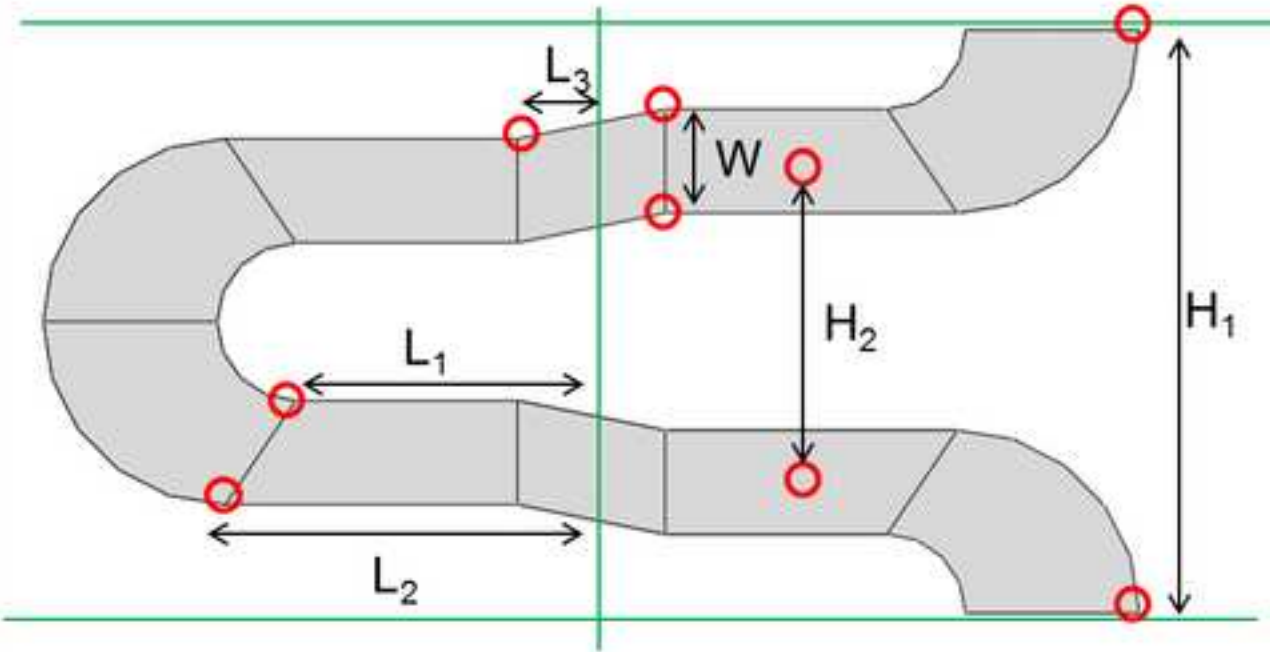


Figure 3a

[Click here to download high resolution image](#)

Variable	Lower Bound (mm)	Upper Bound (mm)
$L_1$	0.3	0.5
$L_2$	$1.0 \times L_1$	$1.2 \times L_1$
$L_3$	0.05	0.25
$H_1$	0.785	0.785
$H_2$	0.393	0.465
$W$	0.11	0.16
$T$	0.11	0.14



### Figure 3b

[Click here to download high resolution image](#)

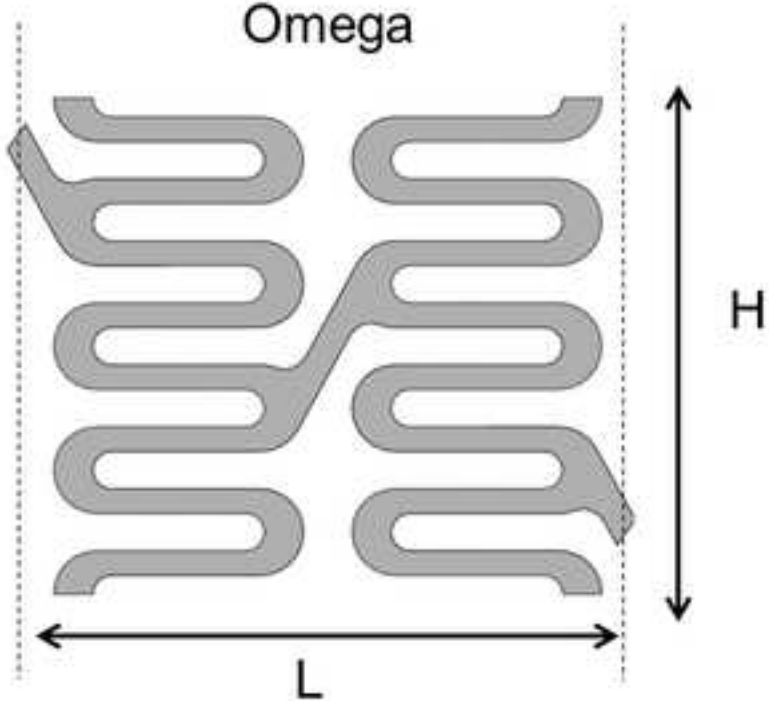


Figure4

[Click here to download high resolution image](#)

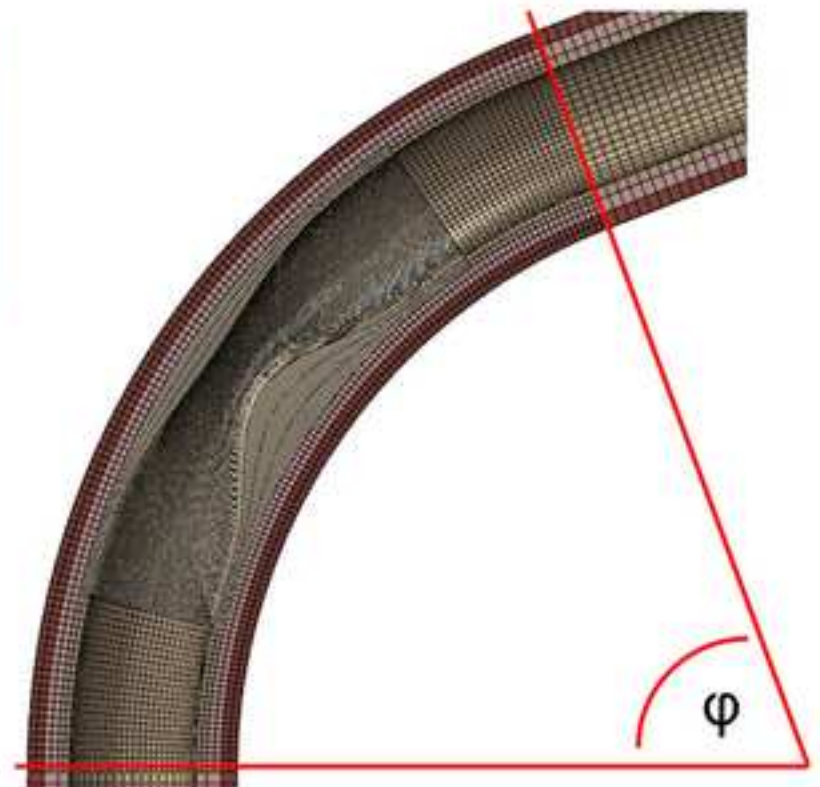
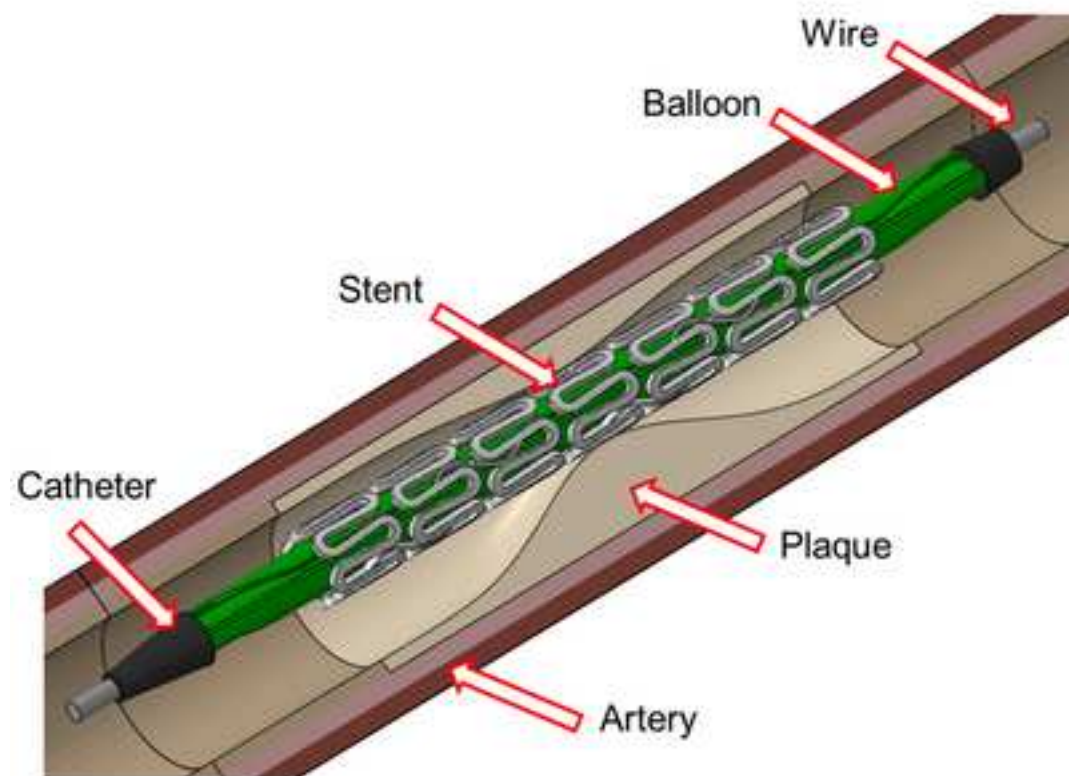


Figure 5a  
[Click here to download high resolution image](#)

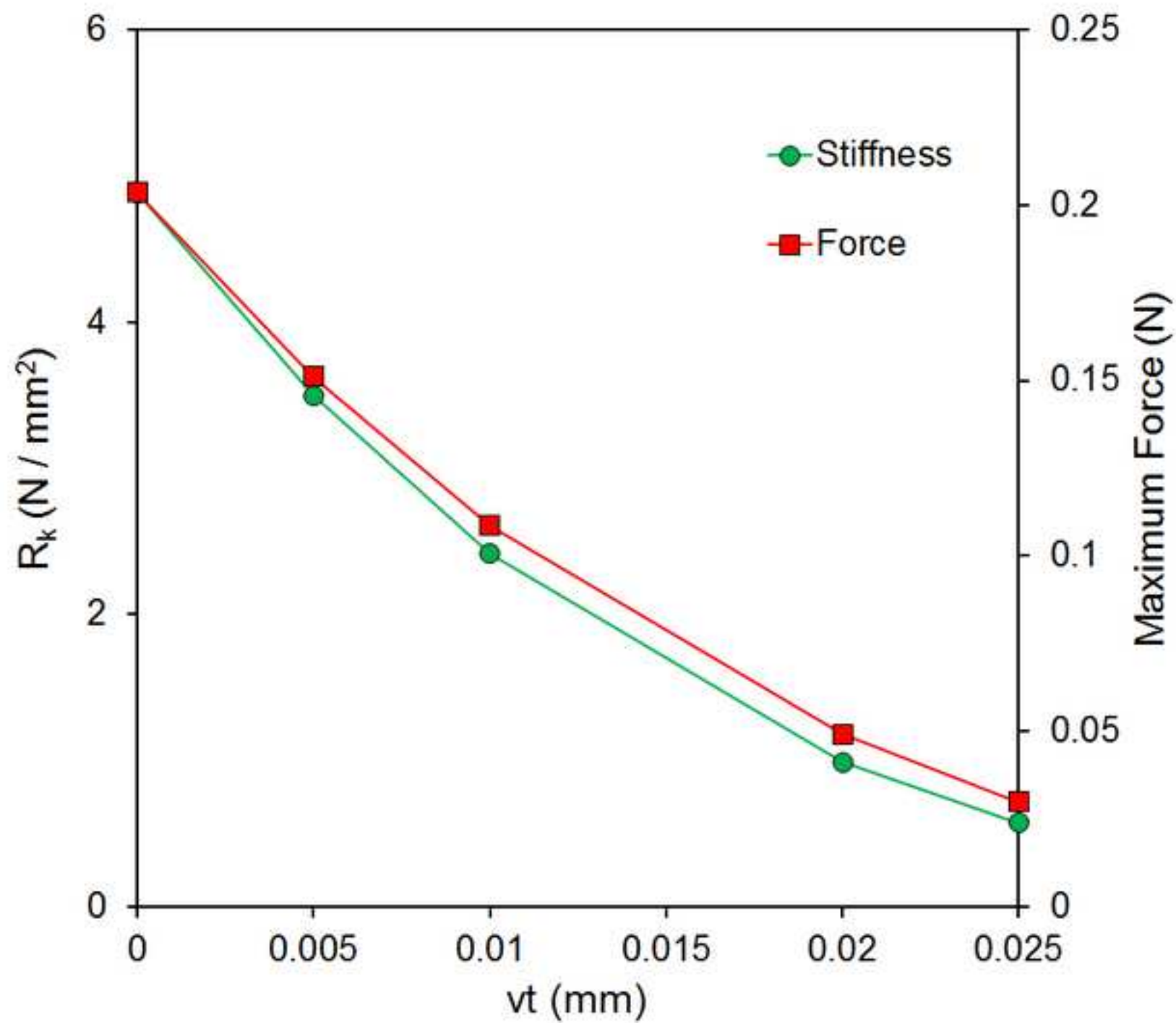


Figure 5b

[Click here to download high resolution image](#)

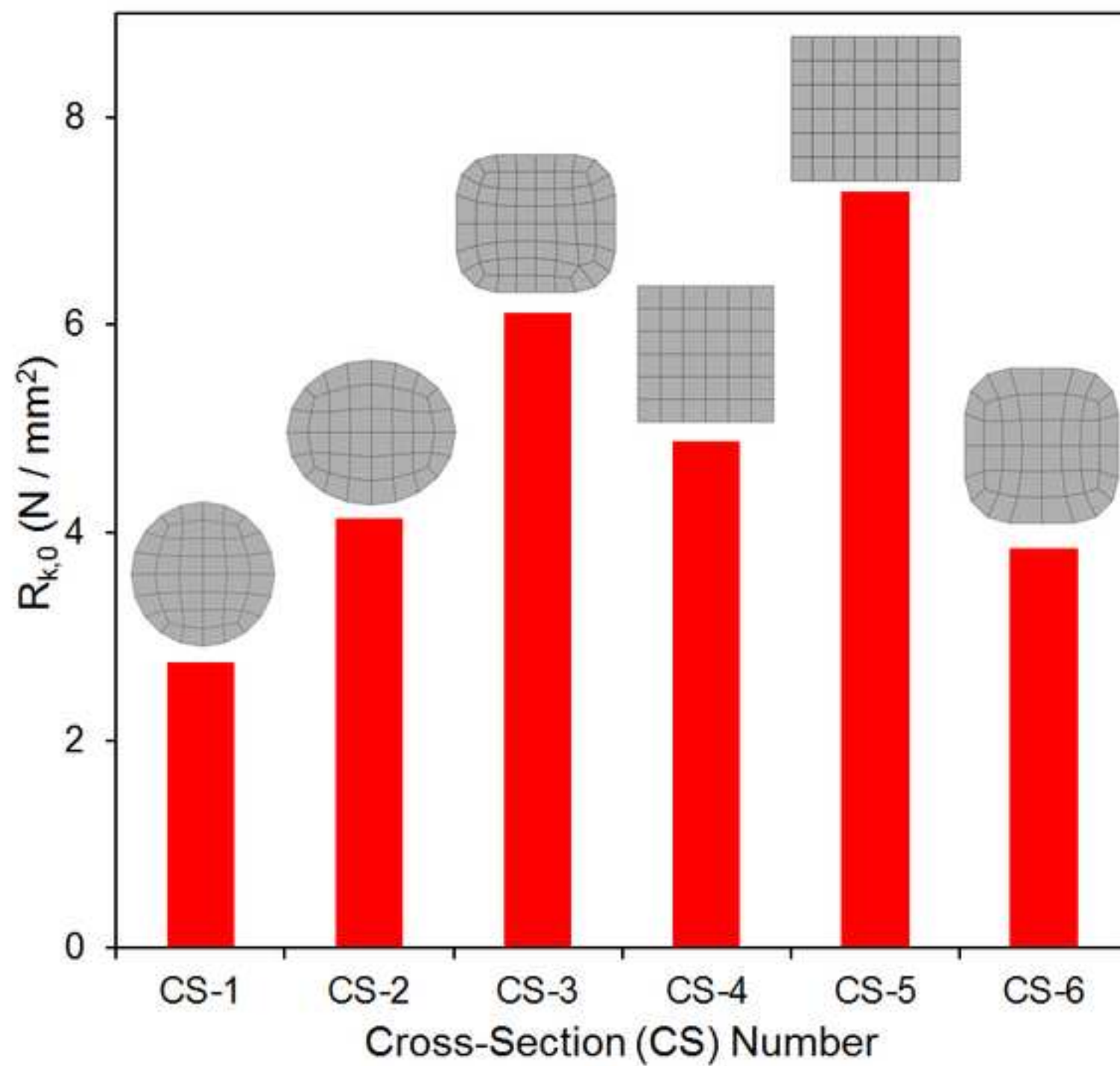




Figure 5c  
[Click here to download high resolution image](#)

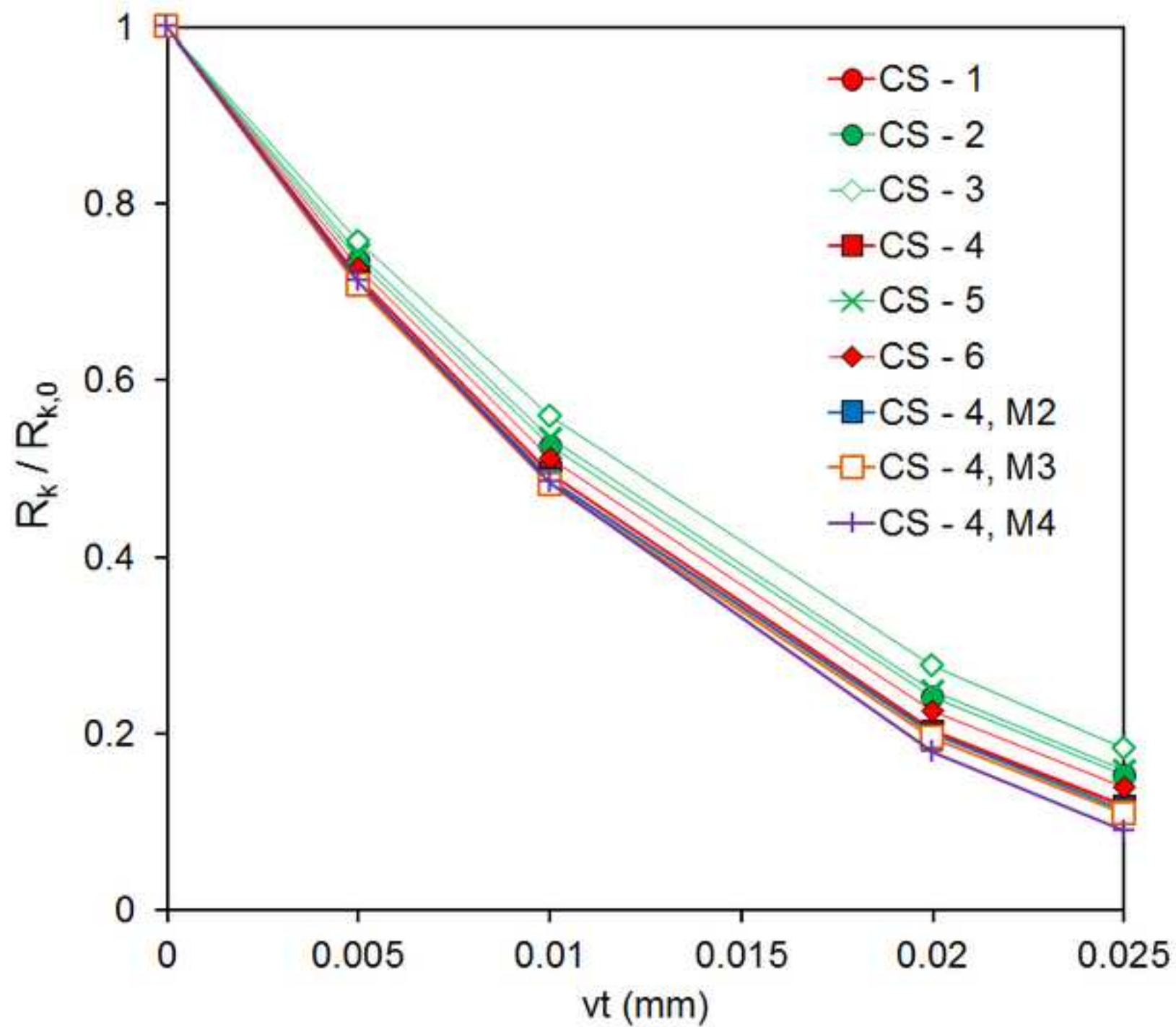




Figure 5d  
[Click here to download high resolution image](#)

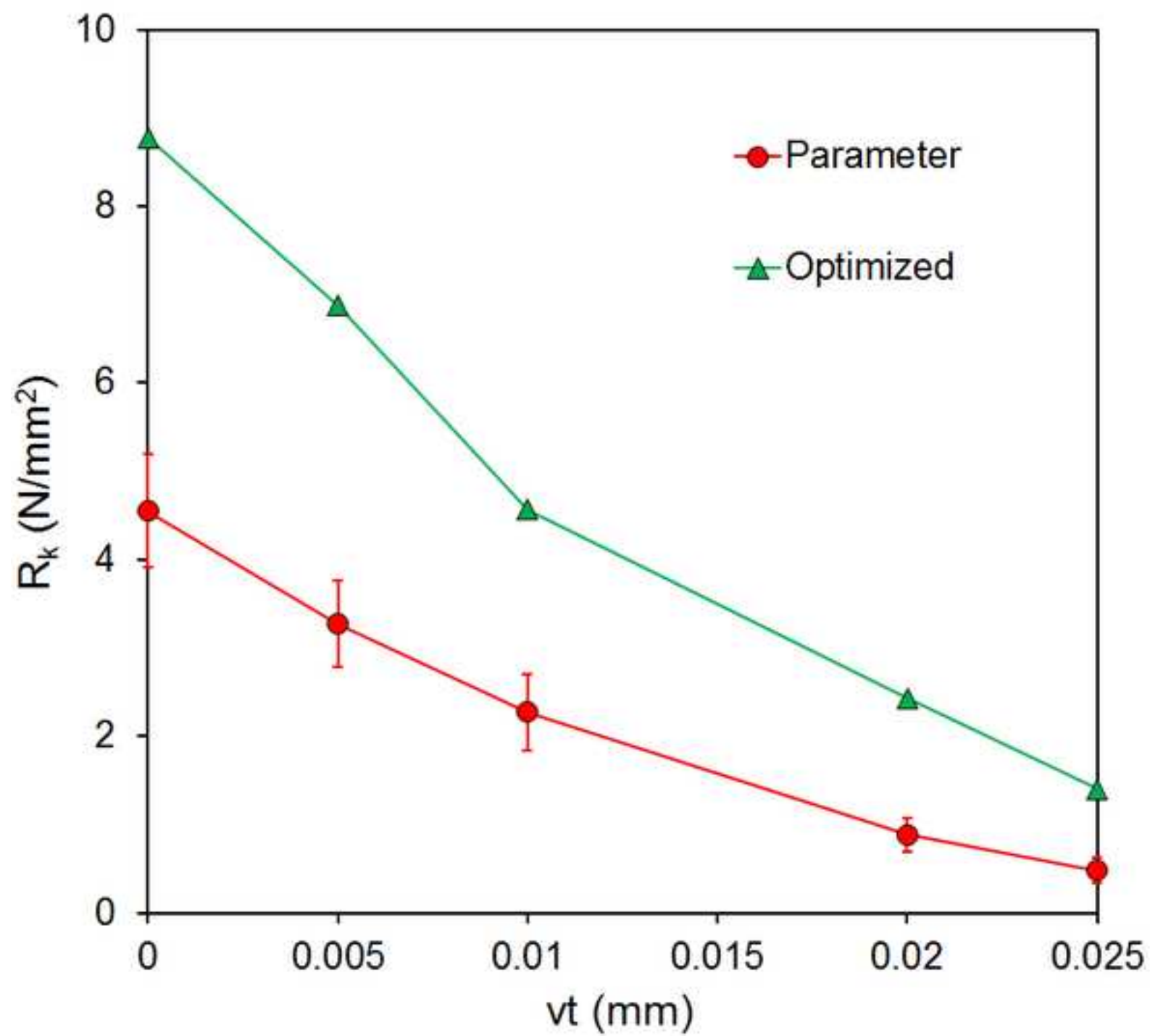


Figure 6a  
[Click here to download high resolution image](#)

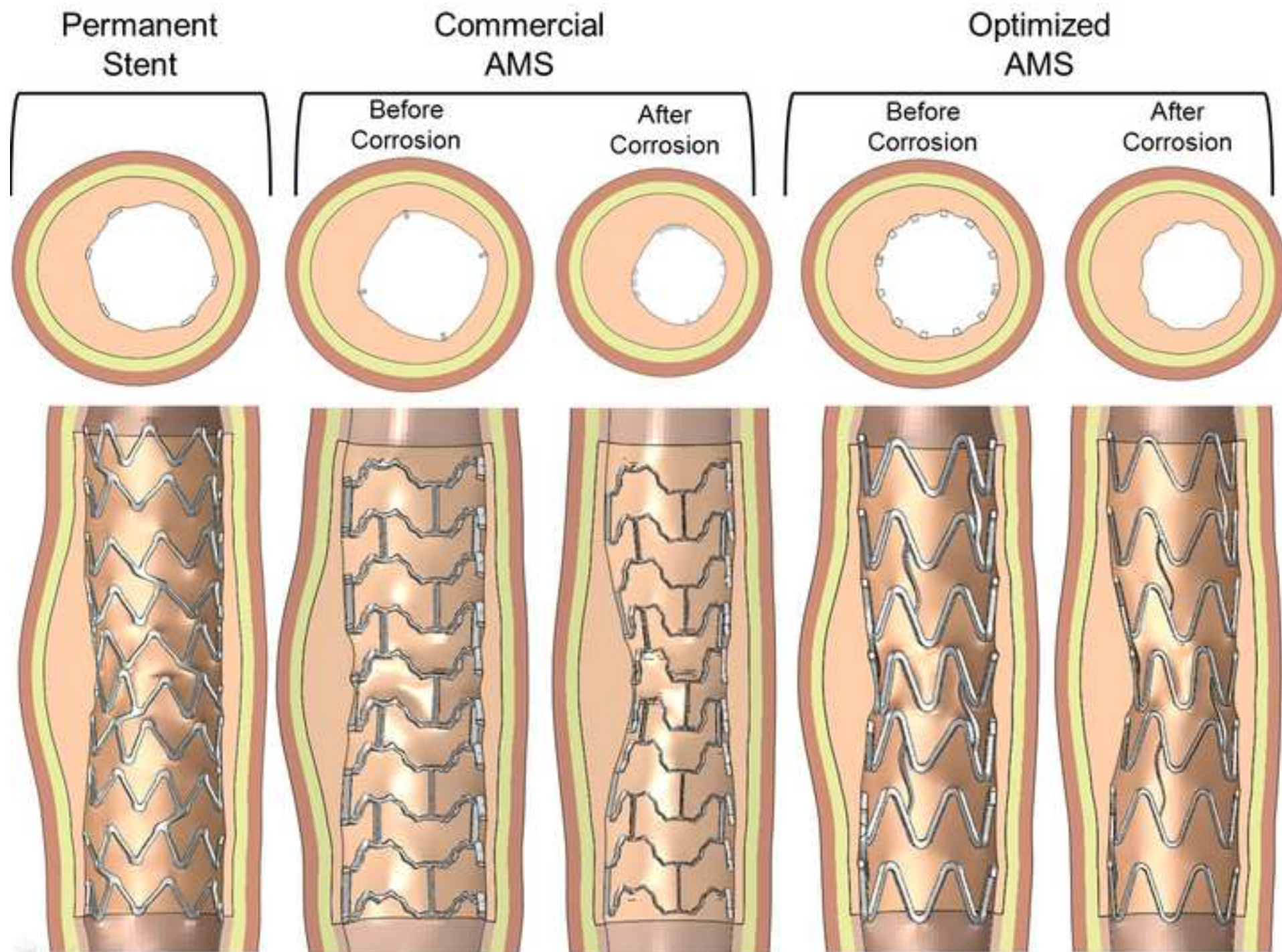


Figure 6b

[Click here to download high resolution image](#)

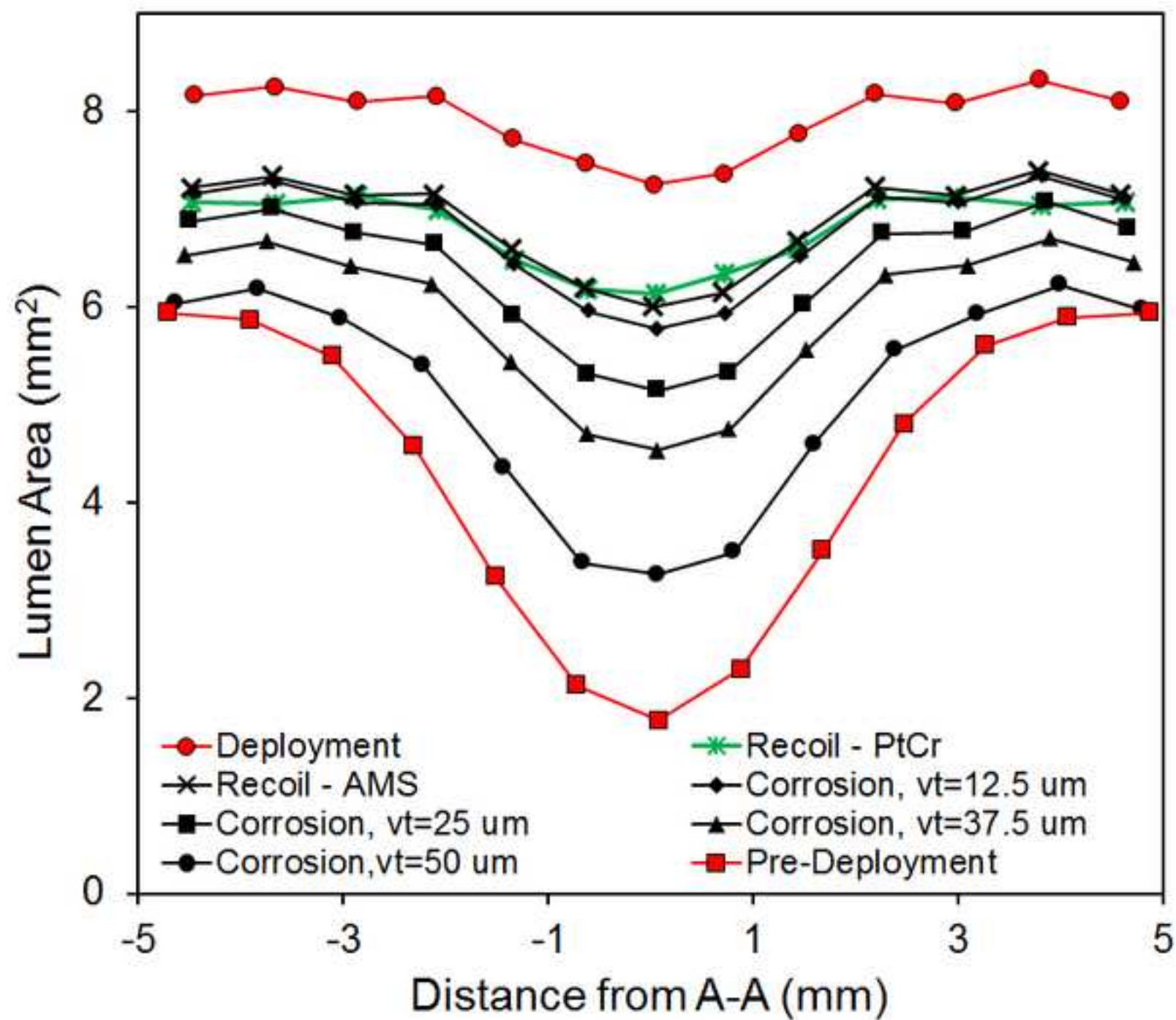




Figure 6c  
[Click here to download high resolution image](#)

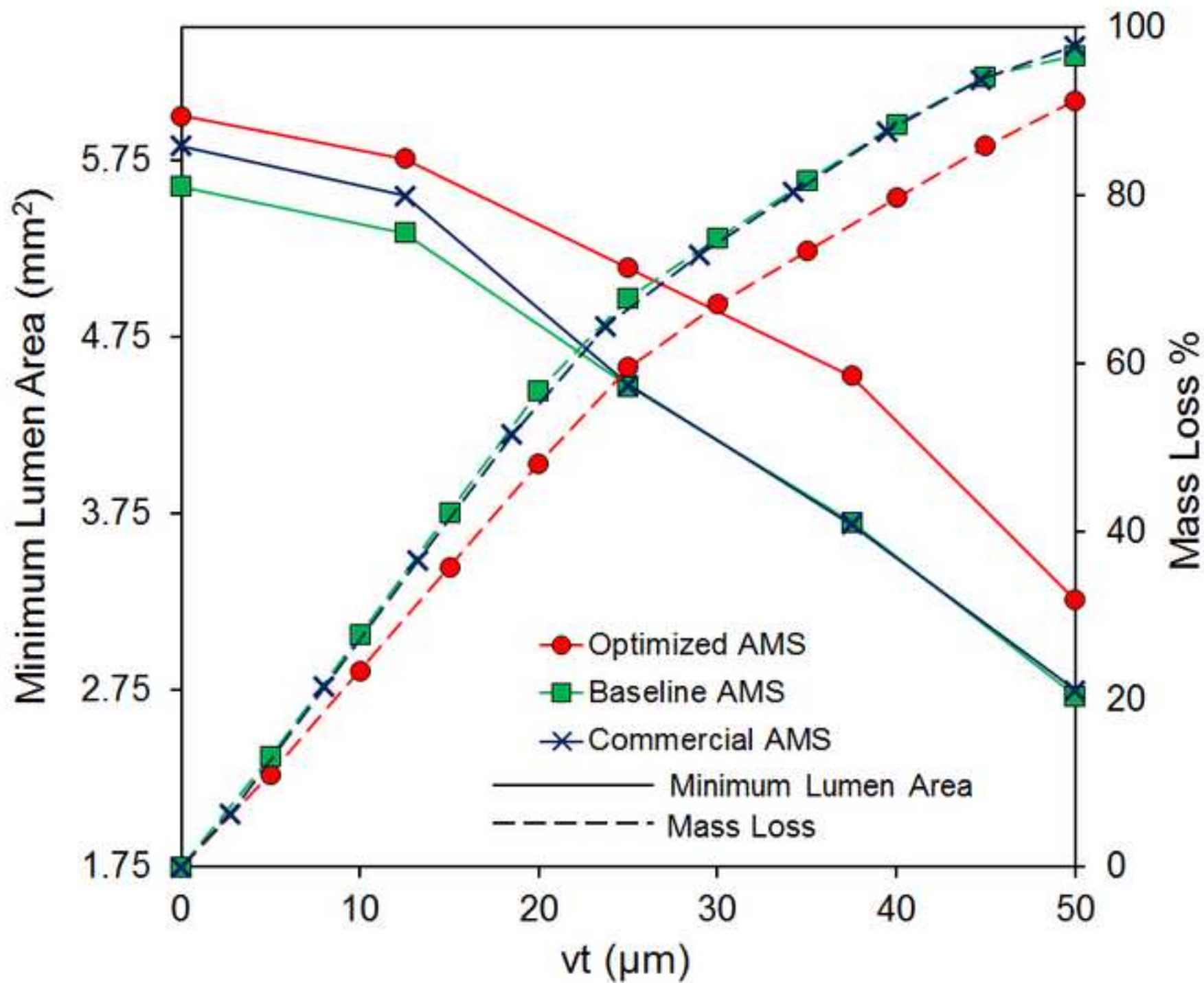


Figure 7a  
[Click here to download high resolution image](#)

Before Corrosion

Uniform Corrosion

Pitting Corrosion

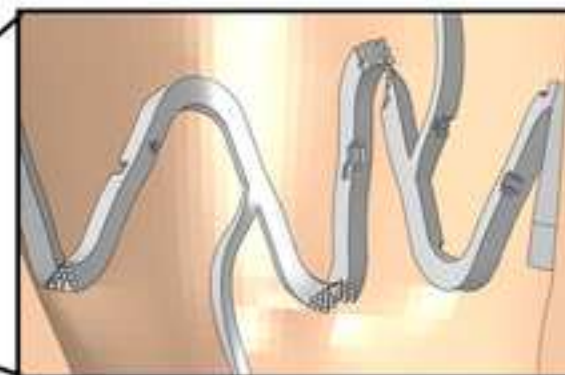
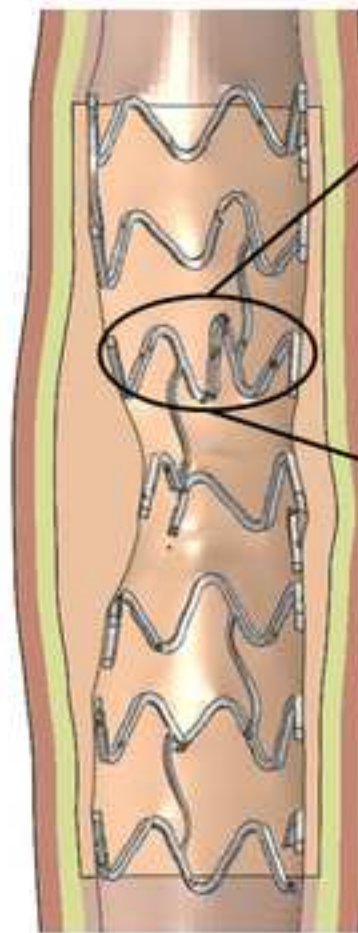
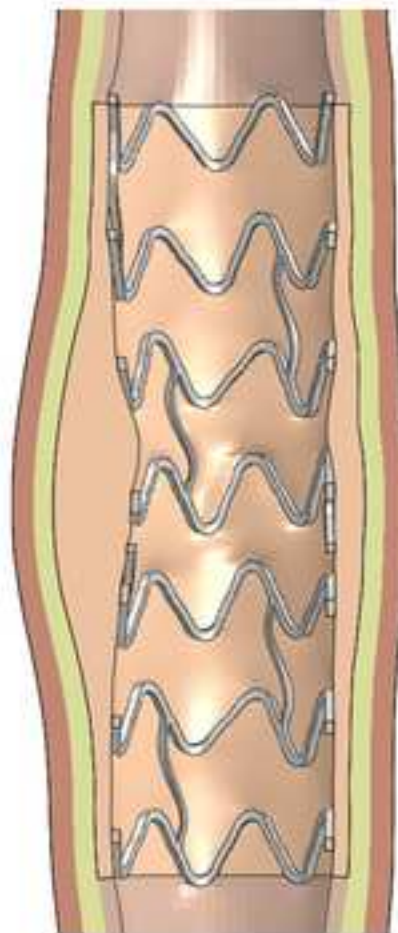
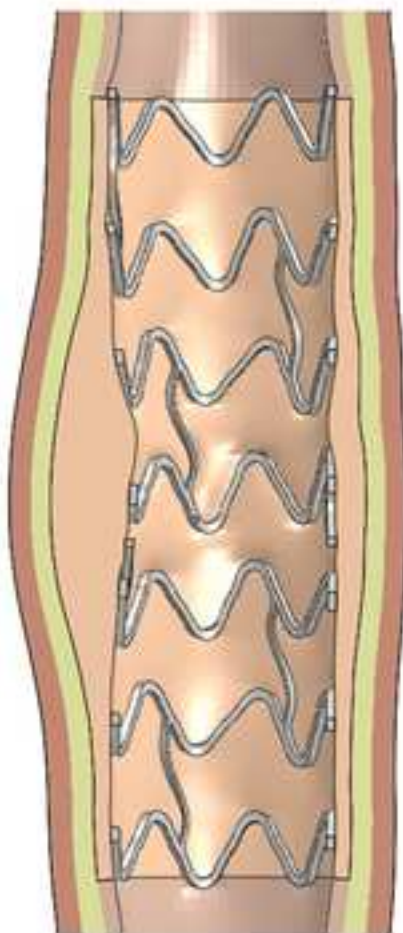
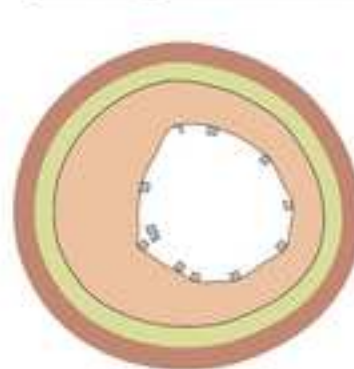
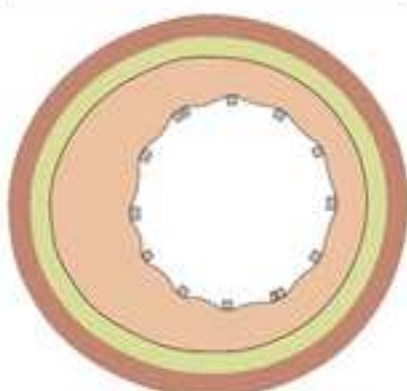
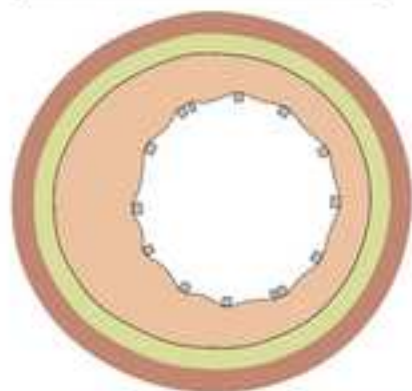


Figure 7b

[Click here to download high resolution image](#)

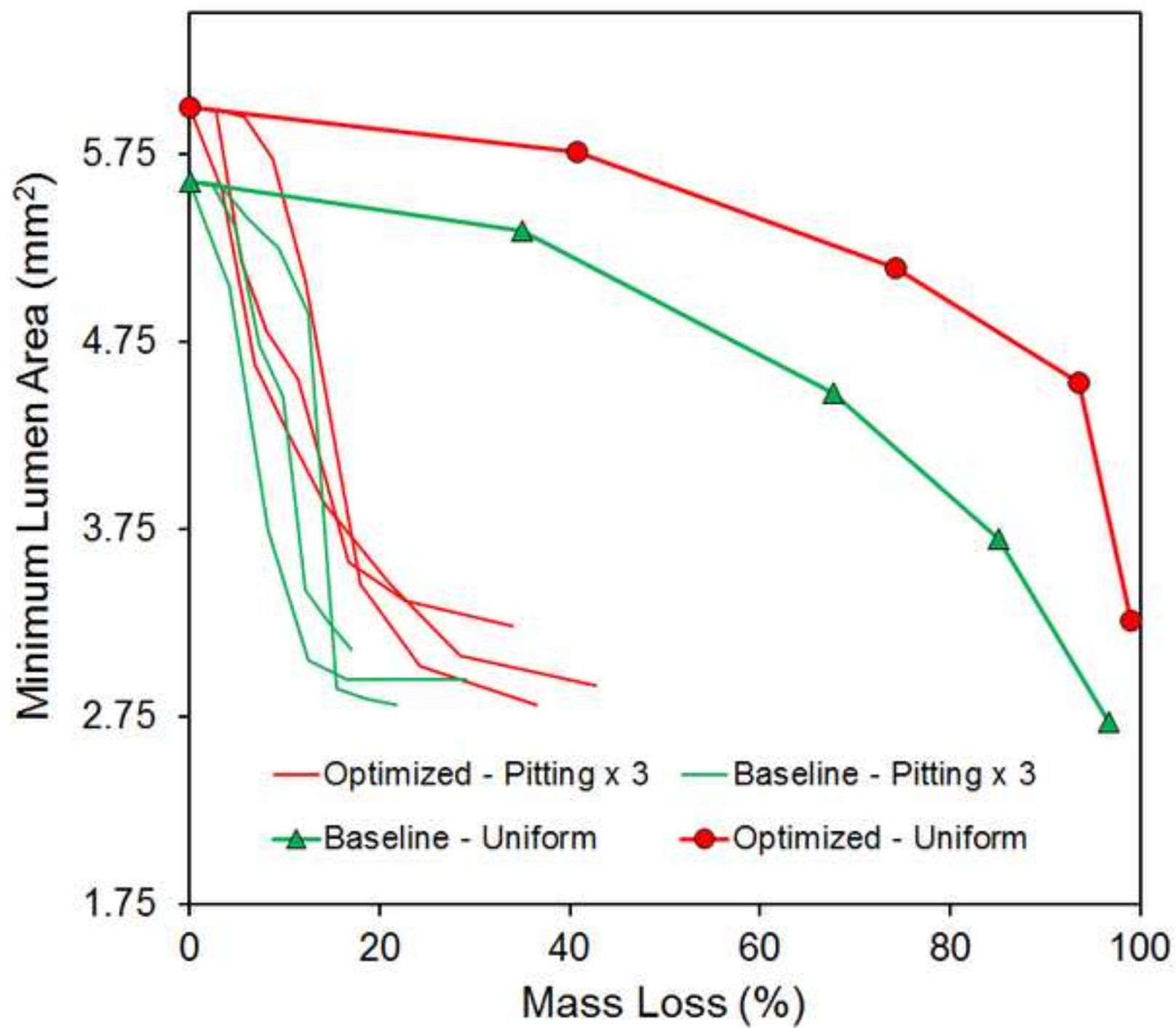


Figure 7c  
[Click here to download high resolution image](#)

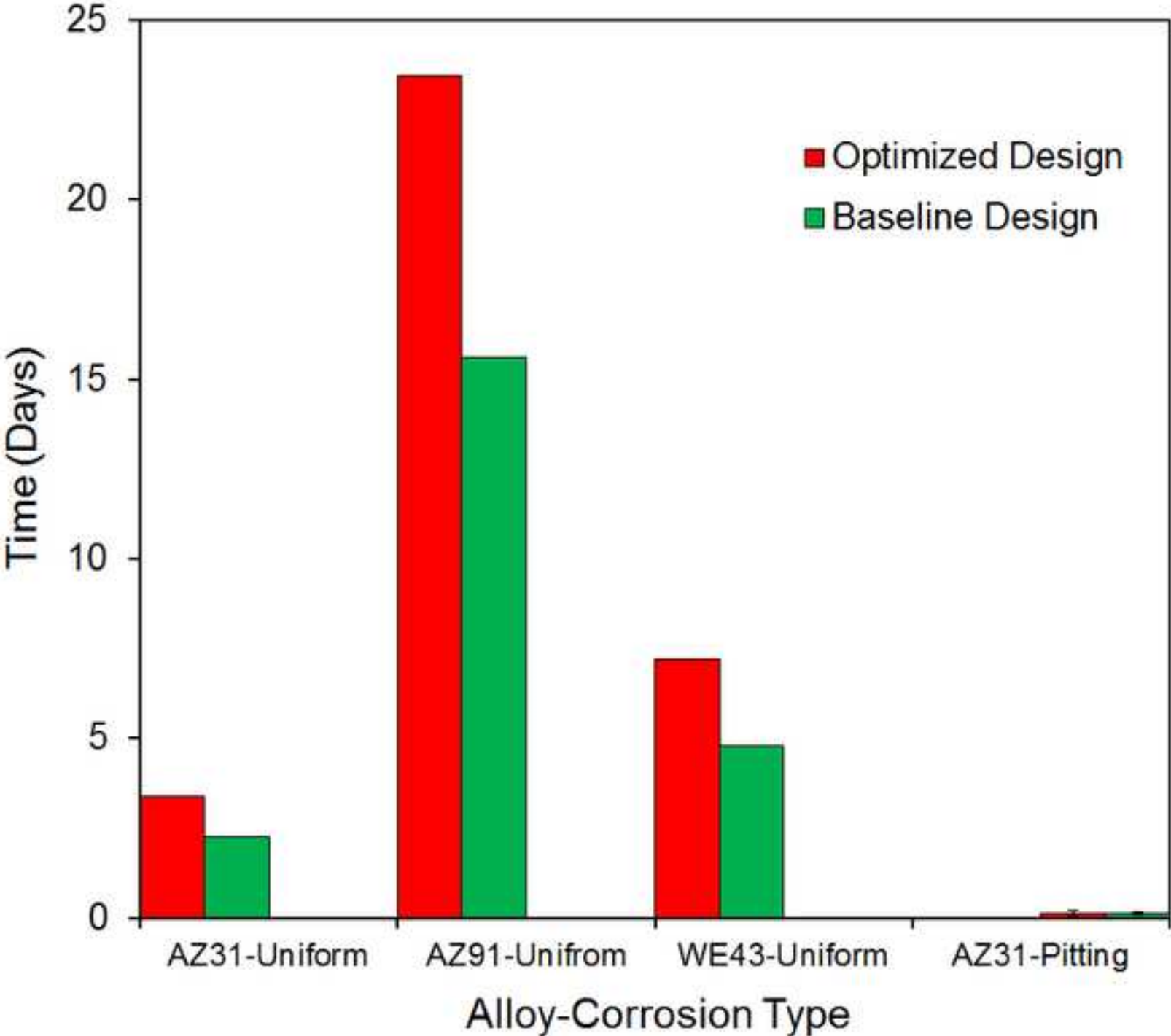
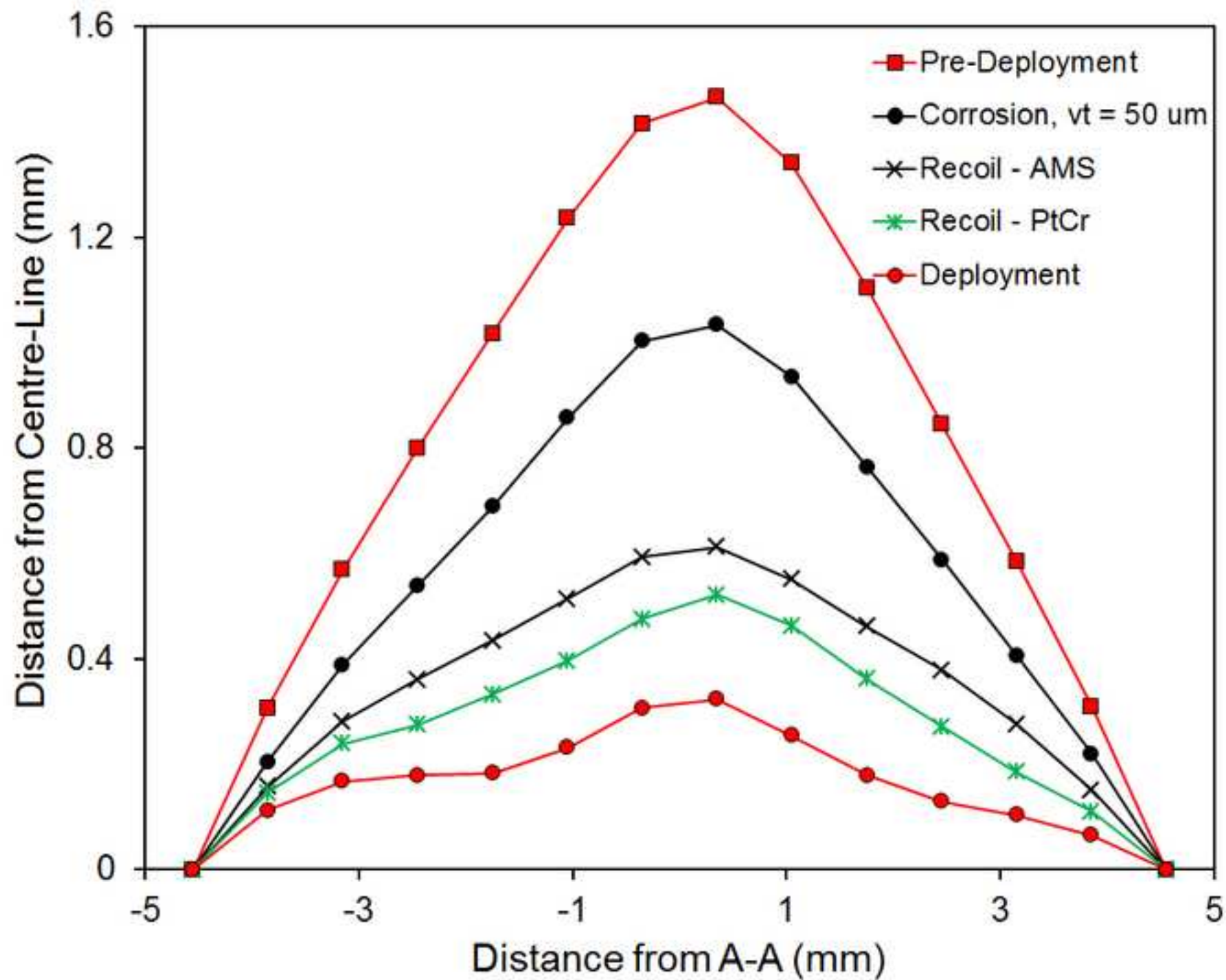




Figure 8  
[Click here to download high resolution image](#)





Tables

Table 1. Engineering stress-strain data used in this study.

Material	E (GPa)	Yield Stress (MPa)	UTS (MPa)	Strain at UTS	Source
PtCr (M1)	203	480	834	44.8 %	O’ Brien et al. [40]
WE43 (M2)	44	216	298	18.5 %	Gu et al. [41]
MZX (M3)	44	184	287	23.0 %	Deng et al. [20]
Iron (M4)	211	170	270	36.0 %	Islam et al. [42]

Table 2. True stress-strain data for AZ31 alloy used in this study, from Grogan et al. [10].

Stress (MPa)	Plastic Strain
138	0.000
170	0.009
192	0.020
231	0.054
271	0.111
288	0.157

Table 3. Information on the components of the stent delivery system used in this study. Material properties are taken from Mortier et al. [7].

	Dimension	Material	FE Mesh (Number of Elements; Element Type)
Balloon	Length = 16.0 mm	Nylon, E = 750 MPa, $\nu$ = 0.4	14,400; M3D4R
Wire	Diameter = 0.34 mm	Nitinol, E = 62 GPa, $\nu$ = 0.3	4,000; C3D8R
Catheter		HDPE, E = 1 GPa, $\nu$ = 0.4	3,440; C3D8R

Table 4. Information on the components of the tissue used in this study. Thicknesses and constants  $\mu$ ,  $k_1$ ,  $\rho$  and  $\phi$  are given by Holzapfel et al. [29]. The plaque constants are given by Gastaldi et al. [30].

Artery Layer	Thickness (mm)	$\kappa$ (kPa)	$\mu$ (kPa)	$k_1$ (kPa)	$k_2$	$\rho$	$\phi$ (deg)	FE Mesh (Number of Elements; Element Type)
Intima	0.24	70.0	28.62	124.01	180.43	0.55	69.5	16,000; C3D8R
Media	0.32	1063.8	0.94	13.28	10.81	0.25	21.0	16,000; C3D8R
Adventitia	0.34	247.5	4.04	32.50	103.63	0.65	72.7	16,000; C3D8R
	$\kappa$ (kPa)	C10 (kPa)	C20 (kPa)	C30 (kPa)	C40 (kPa)	C50 (kPa)	C60 (kPa)	
Plaque	4762	2.38	189	-388	3,730	-2,540	573	53,000; C3D8R

Table 5. Optimized and Baseline device dimensions, based on the geometry in Fig. 3. The result of the fifth optimization (Opt 5) is taken as the overall optimal design.

	$L_1$ (mm)	$L_2$ (mm)	$L_3$ (mm)	$H_1$ (mm)	$H_2$ (mm)	W (mm)	T (mm)	Objective Function
Opt 1	0.406	1.036	0.100	0.785	0.435	0.131	0.137	0.714
Opt 2	0.410	1.044	0.374	0.785	0.421	0.132	0.140	0.682
Opt 3	0.456	1.031	0.456	0.785	0.442	0.139	0.140	0.697
Opt 4	0.408	1.033	0.106	0.785	0.410	0.133	0.136	0.683
Opt 5	<b>0.451</b>	<b>1.053</b>	<b>0.500</b>	<b>0.785</b>	<b>0.393</b>	<b>0.143</b>	<b>0.140</b>	<b>0.670</b>
Baseline	<b>0.319</b>	<b>1.100</b>	<b>0.184</b>	<b>0.785</b>	<b>0.431</b>	<b>0.114</b>	<b>0.117</b>	

**Supp Figure 1**  
[Click here to download Supplementary Files: S1.tif](#)

## Supp Figure 2

[Click here to download Supplementary Files: S2.tif](#)

### Supp Figure 3

[Click here to download Supplementary Files: S3.tif](#)

## Supp Figure 4

[Click here to download Supplementary Files: S4.tif](#)

**Supp Figure 5**  
[Click here to download Supplementary Files: S5.tif](#)

Movie/Animation 1

[Click here to download Movie/Animation: M1.avi](#)



Movie/Animation 2

[Click here to download Movie/Animation: M2.avi](#)

**Movie/Animation 3**

**[Click here to download Movie/Animation: M3.avi](#)**

# Video Still 1

[Click here to download high resolution image](#)

